



Universidad
Carlos III de Madrid



UNIVERSITY of CALIFORNIA, SAN DIEGO
MEDICAL CENTER MOORES CANCER CENTER

Higher Polytechnic School

DEPARTMENT OF THERMAL ENGINEERING AND FLUIDS MECHANICS

TOWARDS A BIOMECHANICAL MODEL OF THE HUMAN LUNG

UNDERGRADUTE FINAL THESIS

AUTHOR: GLORIA NUÑEZ MARQUEZ

SUPERVISORS:

LAURA CERVIÑO

JAVIER RODRIGUEZ

Leganés, Octubre 2011

Title: TOWARDS A BIOMECHANICAL MODEL OF THE LUNG

Author: Gloria Núñez Márquez

Director: Javier Rodríguez Rodríguez

THE TRIBUNAL

President: _____

Vocal: _____

Secretary: _____

Performing the act of defense and dissertation the Final Project on 27th of October 2011 in Leganés, at the Higher Polytechnic School of the Carlos III University of Madrid, agrees giving the GRADE of:

VOCAL

SECRETARY

PRESIDENT

AKNOWLEDGMENT

I would like to acknowledge to my project supervisors: Laura Cerviño, from University of California, San Diego, she has helped me during these 5 months in UCSD, and the time before I went, supporting me and teaching me about medical physics. My second supervisor and this project's director, Javi Rodriguez from University Carlos III of Madrid, for his help, guidance, and all good moments we spent together. Thanks to both because they have made this project possible offering to me the opportunity to do so.

I would also like to thank the entire "CART" research team for help, collaboration, and inspiration. In particular I would like to thank to Reza Shirazi from the biomechanical department at UCSD, for his patience through the endless questions I asked him.

I would like to express my gratitude to all people in my family who has supported me during all these years studying, specially to my grandparents, my uncle and my parents because they always encouraged me to keep going.

It is impossible to forget my gratitude to all people who I met in San Diego, because all of them made my stay there an unforgettable experience. Mainly I would like to thank to my roommates, Max, for all his support during the hardest part in my work; and Austin Kuo, for all the help he still keeps offering me and all good and funny moments we spent together, which for sure will be repeated soon.

I would like to acknowledge to all these people who accompany me during this long path, for all stress situations and joys and sorrows shared. They are a lot, and I'm not writing down all their names, but they know they are there. Especially I have to say thanks to Pablo, for teaching me to not give up in these six years.

I would like to mention a person who I know since we were very young, and she is going to be glad to find her name written here, Laura Cubero, because I know it will be saved as "letter for the posterity".

And finally I would like to thank to all people that have given me their trust and support and helped to make possible this project.

ABSTRACT

Radiotherapy of the lung is challenging due to the motion induced by respiration. Plans of radiotherapy treatments are developed based on static computed tomography (CT) images, while treatment is performed in moving organs. This leads to a lack of precise knowledge of the actual position of the tumor and internal organs during treatment makes the calculation of actual dose absorbed by the lungs and surrounding tissues unknown.

In the Center for Advanced Radiotherapy Technologies (CART), the research arm of the Department of Radiation Oncology at University of California San Diego (UCSD, Moores Cancer Center) sets a goal: Improving lung radiotherapy using Adaptive Radiation Therapy (ART). This consists of knowing the actual dose of radiation delivered during the treatment so that when needed it should be possible to adjust the dose absorbed by the tumor to the dosage prescribed by the oncologist.

In this context, a well-defined model of the organ, and that conforms to the anatomical and physiological characteristics of it is proposed. The project proposed here is based on developing a biomechanical model of the lungs using finite elements (FE). From 4D CT patient's data sets, we obtain geometric characteristics of the organ. Biomechanical properties are optimized in order to obtain the desired movement of internal body identified in the images.

From the numerical model, we apply loads and boundary conditions that lead to the final state of the lung at the breathing process. Overall, it is a three-dimensional mechanical system which aims to achieve a final geometry known beforehand.

With this proposed biomechanical model of the lungs, the internal anatomy may be obtained at each instant in the breathing cycle. The knowledge of the anatomy and the radiation beam, along with a dose calculation algorithm, allow calculating the instantaneous real dose delivered to the patient at each moment, which is a step in adaptive radiation.

Keywords: *4D CT, Respiratory motion, mesh generation, mesh smoothing, biomechanical properties, finite elements.*

RESUMEN

La radioterapia del pulmón es un reto debido al movimiento inducido por la respiración. Las planificaciones de los tratamientos de radioterapia se desarrollan sobre la base de imágenes estáticas de tomografías computarizadas (CT), mientras que el tratamiento real se lleva a cabo en los órganos en movimiento. Esto conlleva a una falta de conocimiento preciso de la posición real del tumor y los órganos internos durante el tratamiento hacen del cálculo de la dosis real que absorben los pulmones y los tejidos circundantes algo desconocido.

En el Centro de Tecnologías Avanzadas de Radioterapia (CART), el brazo de investigación del Departamento de Radiología Oncología de la Universidad de California, San Diego (UCSD, Moore centro para el cáncer) se plantea un objetivo: mejora de la radioterapia del pulmón mediante la radioterapia adaptativa (ATR). Esto consiste en conocer la dosis real de radiación suministrada durante el tratamiento de manera que cuando, sea necesario, sea posible ajustar la dosis real absorbida por el tumor a la dosis prescrita por el oncólogo.

En este contexto, es necesario partir de un modelo del órgano bien definido, y que se ajuste a las características anatómicas y fisiológicas del mismo. El proyecto que aquí se propone se basa en el desarrollo un modelo biomecánico de los pulmones por medio de elementos finitos (FE). A partir de conjuntos de datos 4D CT del paciente se obtendrán las características geométricas del órgano. Las propiedades biomecánicas serán optimizadas para obtener el movimiento deseado del órgano interno identificado en las imágenes.

A partir del modelo numérico, se aplicarán cargas y condiciones de contorno que lleven al pulmón desde el estado inicial del proceso de la respiración, hasta el estado final. En conjunto, se trata de un sistema mecánico tridimensional en el que se pretende conseguir una geometría final conocida de antemano.

Con este modelo biomecánico de los pulmones propuesto se podrá obtener la anatomía interna a cada instante en el ciclo de la respiración. El conocimiento la anatomía y el haz de radiación, junto con un algoritmo de cálculo de dosis, permiten calcular la dosis instantánea en el paciente en cada instante, lo que supone un paso para la radioterapia adaptativa.

Palabras clave: *4D CT, movimiento respiratorio, generación de la malla, suavizado de la malla, propiedades biomecánicas, elementos finitos.*

TABLE OF CONTENT

AKNOWLEDGMENT	v
ABSTRACT	vii
RESUMEN	viii
TABLE OF CONTENT	x
FIGURE INDEX	xii
TABLE INDEX	xiii
GRAPH INDEX	xiv
ABBREVIATIONS INDEX	xv
 PART I: INTRODUCTION	 16
1. INTRODUCTION AND AIMS	16
1.1. Overview and problem description	16
1.2. Objectives	18
1.3. Content	18
2. RADIATION THERAPY	21
3. RESPIRATORY SYSTEM	24
3.2. Breathing Process	30
4. 4D CT	32
 PART II: LUNG MODEL	 34
1. MODEL EQUATIONS	34
2. FINITE ELEMENTS METHODS	38
3. OBTAINING DATA	44
4. MESH GENERATION	47
4.1. Overview	47
4.2. Implementation	51
4.3. Results	52
5. SMOOTHING	57
5.1. Overview	57
5.2. Implementation	61

5.3. Results	63
6. LUNG FINAL MODEL	73
PART III: SIMULATION	76
1. NUMERICAL MODEL	76
2. SIMULATION RESULTS.....	82
PART IV: COMPARISON WITH OTHER TECHNIQUES.....	85
1. DEFORMABLE REGISTRATION	85
2. COMPARISON.....	88
PART V: CONCLUSIONS AND FUTURE WORKS	93
1. SIGNIFICANCE AND INNOVATION OF A BIOMECHANICAL MODEL OF THE LUNGS	93
2. HOW TO IMPROVE THE MODEL.....	95
APENDIX A: Iso2mesh.....	98
APENDIX B: Planning and budget	99
REFERENCES	104

FIGURE INDEX

FIGURE I. 1: Work Flow.....	19
FIGURE I. 2: Linear Accelerator.....	21
FIGURE I. 3: Radiation Therapy planning	23
FIGURE I. 4: Main organs in the respiratory system	24
FIGURE I. 5: Fissure and lobes of the lung	26
FIGURE I. 6: Bronchial tree scheme	27
FIGURE I. 7: Internal airways.....	29
FIGURE I. 8: Inspiration and expiration.....	31
FIGURE II. 1: Principle and terminology.....	35
FIGURE II. 2: Encastred Beam	38
FIGURE II. 3: 4D CT 10 breathing phases	44
FIGURE II. 4: ECLIPSE snapshot	45
FIGURE II. 5: Delaunay triangulation	47
FIGURE II. 6: Delaunay's criteria	48
FIGURE II. 7: Flipping edge	48
FIGURE II. 8: Steps 1 and 2 in Delaunay algorithm	50
FIGURE II. 9: Shape factor	52
FIGURE II. 10: Mesh sizes.....	53
FIGURE II. 11: Direct Neighborhood.....	59
FIGURE II. 12: Laplacian algorithm.....	60
FIGURE II. 13: Meshed lung	62
FIGURE II. 14: Laplacian algorithm smoothing results. $\lambda = 0.7$	65
FIGURE II. 15: Five iteration smoothing for laplacian hc algorithm.....	67
FIGURE II. 16: Laplacian hc algorithm smoothing result. $\lambda = 0.7$	68
FIGURE II. 17: Low pass algorithm smoothing results. $\lambda = 0.5$	72
FIGURE II. 18: Lung internal meshing.....	73
FIGURE III. 1: EE and EI states	79
FIGURE III. 2: Normal vectors.....	80
FIGURE III. 3: Pressure 1 and bottom surface.	81
FIGURE III. 4: Displacement vectors.....	82
FIGURE III. 5: Displacement field magnitude	83
FIGURE III. 6: Contact open	83
FIGURE IV. 1: Landmarks	88
FIGURE A.B. 1: Gantt Diagram of the process.....	100

TABLE INDEX

TABLE I. 1: Description of the main organs in the respiratory system	25
TABLE II. 1: Meshing results.....	53
TABLE II. 2: Fundamental artifacts in medical imaging.....	58
TABLE II. 3: Computational time in seconds for laplacian smoothing	65
TABLE II. 4: Computational time in seconds for laplacian hc smoothing	68
TABLE II. 5: Computational time in seconds for low pass smoothing	71
TABLE II. 6: Smoothing methods	71
TABLE II. 7: Mesh quality values.....	74
TABLE II. 8: Mechanical properties in the literature.....	74
TABLE IV. 1: Landmarks positions at EE and EI and displacement vectors	89
TABLE IV. 2: Comparison of the displacements.....	90
TABLE A.B. 1: Budget.....	102

GRAPH INDEX

GRAPH II. 1: Shape functions.....	39
GRAPH II. 2: AR vs. Mesh size.....	54
GRAPH II. 3: Sf. vs. Mesh size	54
GRAPH II. 4: Worst SF vs. Mesh Size	55
GRAPH II. 5: Worst AR vs. Mesh size.....	55
GRAPH II. 6: SF vs. Iterations in Laplacian smoothing.....	63
GRAPH II. 7: Degree of shrinkage vs. iterations in laplacian smoothing.....	64
GRAPH II. 8: SF vs. Iterations in laplacian hc smoothing	66
GRAPH II. 9: degree of shrinkage vs. Iterations in laplacian hc algorithm	67
GRAPH II. 10: SF vs. Iterations in low pass smoothing	69
GRAPH II. 11: Degree of shrinkage vs. Iterations in low pass smoothing.....	70
 GRAPH III. 1: Lung volume in every breathing phase	 77
GRAPH III. 2: Breathing curve	78
 GRAPH IV. 1: Landmarks displacements comparison.....	 91

ABBREVIATIONS INDEX

CART	Center for Advanced Radiotherapy Technologies
ART	Adaptive Radiation Therapy
UCSD	University of California San Diego
EE	End of Expiration
EI	End of Inhalation
FEM	Finite Elements Methods
3D	Three dimensions
4D	Four dimensions
CT	Computed tomography
SI	Superior-inferior direction
ROI	Region of interest
HC	Humphrey's Classes
SF	Shape Factor
AR	Aspect Ratio
Inmrk	landmark

PART I: INTRODUCTION

1. INTRODUCTION AND AIMS

1.1. Overview and problem description

Lung cancer is amongst the most common malignancies for men and women in the United States. Every year there are about 220,000 new cases and 160,000 deaths. Despite the use of multiple modalities of treatment including surgery, chemotherapy and radiation therapy, the 5 year survival rate is less than 15%. Radiation therapy is widely used in patients who have locally advanced disease, as well as in patients who are medically inoperable. Radiation therapy can also be given to relieve symptoms such as pain or coughing up blood and to open airways obstructed by tumors. Many lung cancer patients will undergo radiation therapy at some point during their treatment.

One of the challenges of radiation therapy for the lung is the presence of motion due to respiration. Although very precise treatment technologies exist for delivering radiation to static tumors, these techniques are not applicable to mobile tumors due to the lack of knowledge of the real-time tumor position and anatomy. In addition, breathing motion leads to treatment planning and treatment delivery inconsistencies

Treatment planning is performed based on an imaging scan of the patient taken prior to therapy. They produce highly blurred images that do not represent a realistic anatomy of the patient or the target position.

Consequently, radiation therapy suffers from missing information regarding organ and tumor mobility. To ensure an adequate dose distribution within the moving tumor, usually the volume to be radiated is expanded. This also increases the volume of radiated healthy tissue and the likelihood of treatment related complications becomes larger, specifically in thoracic tumors, where the target's motion reaches the magnitude of centimeters.

Techniques exist to ensure reproducibility of the anatomy of the patient avoiding risk in surrounding tissues as far as possible; for example, 4DCT, consisting normally of 10 CT scans, corresponds to 10 different breathing phases. Delivering the dose at just one breathing phase appears to be a possible solution, because the tumor's position is well known at this phase. However, delivery of radiation at one breathing phase is highly inefficient in terms of duty cycle, where duty cycle is defined as follows:

$$\text{duty cycle} = dc = \frac{\text{time beam on}}{\text{total treatment time}} \quad (\text{Eq.I.1})$$

Other solution could be breath holding, a technique in which the patient holds their breath for a couple of seconds on a position on the respiration curve. If the patient holds their breath, the quality of acquired data can be improved. Additionally, it can make radiation treatment at one breathing phase possible. However, lung cancer patients have impaired pulmonary function, making it difficult for them to hold their breath.

In addition, even if the patient could be treated at one specified breathing phase, location of the tumor at that same phase might still change, since breathing patterns change from day to day, and even within the same day (for example, the breathing phase could be constant, but breathing amplitude could change, or tumor baseline could drift).

Therefore, for any current technique used to deliver radiation to lung tumors, the received dose will differ from the planned dose.

In conclusion, dose verification is needed to compare real delivered dose to the prescription dose and to modify treatment accordingly when is necessary.

The purpose of the proposed work is to build a framework that can be used to verify the dosage administered during lung radiotherapy treatment. This requires a rigorous knowledge of the patient's anatomy and especially the lung, including its anatomy and its movement due to respiration cycle. The present project focuses on the biomechanical modeling of the lung based on finite element methods (FEM) that can be used as information source in treatment planning. It constitutes one step to real time modeling.

1.2. Objectives

Once the problem is defined, it is necessary to specify the main objectives of this project, since the problem is widespread and the solution is still in development.

This research project will primarily focus on two objectives: the first one serves an **anatomical** focus; it will consist of a three-dimensional (3D) lung volume meshing, which will be used to adequately represent the lung geometry. This mesh will meet a series of meshing criteria that will be defined in the following chapters. This will be achieved through the medical image processing analysis of an anonymous lung cancer patient.

The second objective aims at modeling from the **physiological** point of view the respiratory function of breathing. Through a simplified engineering model system based on forces and movement constraints, we will find the best conditions to represent the process of inspiration/expiration using the finite element method, implemented through specialized commercial software.

1.3. Content

The work flow followed during this project is shown in Figure I.1. Here, different stages of the process can be seen, each of which will be seen in detail in subsequent chapters.

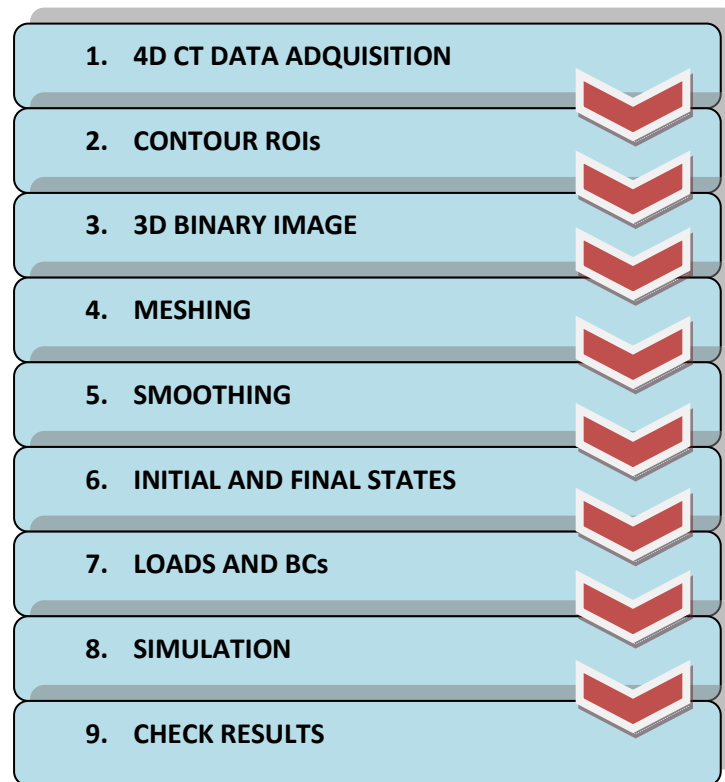


FIGURE I. 1: Work Flow

Main steps in the research process

The text is divided into 5 parts: the first part, the introduction, the main objectives and purposes are explained as well as all the theoretical aspects of the engineering field such as radiology and anatomy, the fundamentals of which are necessary to develop this project.

The second part of the text, the Lung Model, is the main body of this project. It covers the five first steps in the work flow, as well as a brief introduction of the mathematical model.

The third part consists of the simulation process. It comprises steps six, seven and eight from the work flow. The initial block in this part covers steps six and seven consisting of the numerical model: Initial and final states are chosen and the loads and boundary conditions applied. Step number eight corresponds with the main simulation process: the problem is solved using specialized software.

The fourth part focuses on the results. They are displayed and compared to other models. For this propose, a second technique is briefly introduced. This part corresponds to the last stages of the work flow.

Finally, the fifth and final part, gives a general overview of how the whole process is carried out and will give some suggestions about possible improvements in continuing developments the model.

2. RADIATION THERAPY

Along with chemotherapy and surgery, radiation therapy is one of the three main modalities of cancer treatment. Radiation can be used with either palliative or curative purpose, and is often combined with other treatments. It can be used in many situations where surgery is not an acceptable option due to risks of complication. It is estimated that radiation is incorporated into the treatments of over 50% of cancer patients.

Radiation therapy is the delivery of focused high-energy x-rays, gamma rays or subatomic particles. It affects cells that are rapidly dividing—such as cancer cells—much more than those that are not. Most cancers, including lung tumors, are made of cells that divide more rapidly than those in normal lung tissue. Radiotherapy acts by attacking the genetic material—or DNA—within tumor cells, making it impossible for them to grow and create more cancer cells. Normal body cells may also be damaged, but they are able to repair themselves and function properly once again. The key strategy is to give daily doses of radiation large enough to kill a high percentage of the rapidly dividing cancer cells, while at the same time minimizing damage to the more slowly dividing normal tissue cells in the same area. Damage to normal tissues can still cause severe complications, so it is essential to minimize the dose to healthy tissue. The most common type of radiation therapy is external beam radiation therapy:

A compact linear accelerator mounted on a gantry that can rotate around the patient is used to deliver a high energy beam to the patient. An image of a typical linear accelerator is showed in Figure I.2.



FIGURE I. 2: Linear Accelerator

Linear accelerator used to treat patients at the University of California, San Diego

Since radiation can cause significant harm to normal tissues, much work is done during the radiation therapy process in an attempt to achieve an optimal balance between sufficient dose to the target and minimal dose to healthy tissues. The radiation therapy process is an exhaustive topic, the details of which are beyond the scope of this report. However, the fundamentals of the process will be reviewed in this section.

The first step in treating a patient who has been prescribed radiation is to build a patient model upon which the treatment can be planned. This phase of the radiation therapy process is called treatment **simulation**, and is usually based around a computed tomography (CT) scan.

The simulation scan is used to define relationships between the target and important normal critical structures. These relationships are used during the next phase of radiation therapy, **treatment planning**. In treatment planning, the patient model is input into software which also models the treatment machine that will be used. An interactive optimization procedure is used to determine the best beam angles, shapes, and intensities to use in order to deliver a dose which conforms tightly to the target, and does not surpass tolerable dose levels for critical structures.

Together, treatment simulation and planning compose the treatment preparation piece of the radiation therapy process. The next piece is treatment execution.

During treatment execution, the patient will return for treatment multiple times, each time receiving a fraction of their total prescribed dose. The first step in each treatment fraction is **patient positioning**, where the patient must be positioned carefully under the treatment machine in order to match the reference geometry established during treatment planning as closely as possible. Since modern radiation technologies allow for a highly conformal dose to be delivered to the target, there is a significant risk of partially missing and under-dosing the target if the patient is not positioned correctly.

Once the patient has been positioned, the last step is to turn on the radiation beam and **deliver the treatment**. During treatment delivery, it is important to monitor the patient to ensure that the reference geometry established during treatment planning (and matched during patient setup) is maintained throughout the treatment.

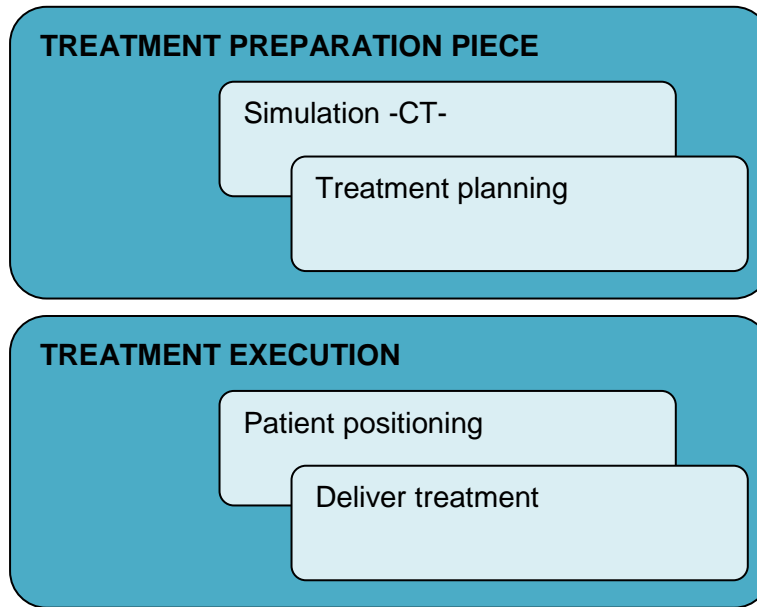


FIGURE I. 3: Radiation Therapy planning

Main procedures in radiotherapy treatments

Organ and target motions cause significant challenges in each step of the radiation therapy process. Motion can occur both between treatments(interfraction motion) and during treatments (intrafraction motion), and has a variety of causes including the cardiac, respiratory, and gastrointestinal systems, weight loss, tumor shrinkage, and skeletal muscular motion.

Optimized treatment plannings must have into account an expected amount of organ motion. Accurate patient setup should account for deformations in patient anatomy, and the target's motion should be monitored and accounted for during treatment delivery. In general, don't have into account the organ motion at the various steps in the radiation process can result in both an under-dosing of the target and in increased dose to normal tissues.

There is a great need for more effective lung cancer therapies.

3. RESPIRATORY SYSTEM

The respiratory system consists of the lungs and airways, which extend from the mouth and nasal cavities into the chest. The airway runs parallel to the upper digestive tract, and the lungs sit within the chest cavity, above the heart and behind the ribcage. The system also includes various accessory muscles that allow air to enter and leave the airways by altering pressure within the chest cavity.

The respiratory system is responsible for gas exchange: it brings oxygen into the lungs and transfers it to the bloodstream so that the oxygen may be pumped through the heart and distributed to the body's cells as life-sustaining fuel. Continuing the cyclical process, the bloodstream carries the carbon dioxide from the body and to the lungs to be expired. This is process we know as **breathing**.

The main organs of the respiratory system are showed in figure I.4 and described in table I.1.

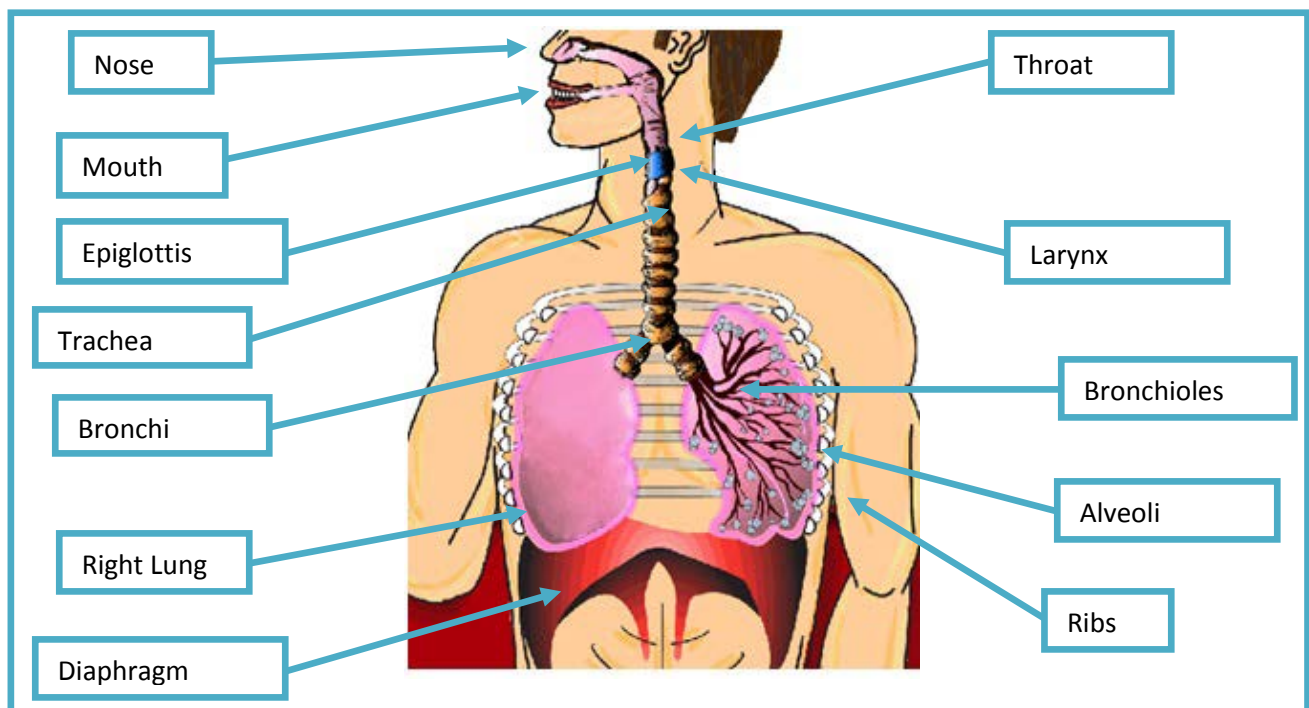


FIGURE I. 4: Main organs in the respiratory system

ORGAN	DESCRIPTION
NOSE	One way that outside air can enter the Respiratory System. The hairs that line the inside wall are part of the air-cleansing system.
MOUTH	Other way that outside air can enter the Respiratory System.
THROAT (pharynx)	Collects incoming air from the nose and mouth and passes it downward to the trachea.
LARYNX or voice box	Contains the vocal cords and is capable of producing vocal sounds during exhalation.
EPIGLOTTIS	Is a flap attached to the entrance of the larynx. It prevents food from going into the trachea.
TRACHEA (windpipe)	Is the passage leading from the throat to the lungs. It divides into the two main bronchial tubes, which lead into each lung.
LUNGS	Are the main organs in the respiratory system. Inside them the bronchial tree is hosted.
BRONCHIAL TREE	Is the trachea and successive branching generations of the respiratory passages. It contains: bronchi, bronchiole, and alveoli ¹ .
RIBS	Are bones that support and protect the chest cavity. They move to a limited degree, helping the lungs to expand and contract.
DIAPHRAGM	Is a wall of strong muscle. By moving downward, it allows air to enter the lungs and by moving upward it pushes air out of the lungs.

TABLE I. 1: Description of the main organs in the respiratory system

3.1. Lungs

Everyone is familiar with the basic functions of the lungs. They allow you to breathe, it's that simple. The average adult takes 15 to 20 breaths a minute – over 20,000 breaths a day.

¹ In order to avoid confusion in nomenclature and multiplicity of these names:

Bronchi is plural, bronchus is singular.

Bronchioli or bronchioles is plural, bronchiole or bronchiolus is singular.

Alveoli is plural, alveolus is singular.

The primary structure is also well known, there are two of them - one on the right and one on the left. But the details of the structure and function of the lungs are somewhat more complicated. The lungs are essential organs in the respiratory system, and also play a minor role in some other bodily functions.

The structure of the lungs

Everyone has two lungs - a right and a left. It is not as well known that the right and left lung are not identical to each other. The lungs are large cone shaped organs which sit on either side of the heart. The apex of the lungs reaches as high as the first rib, which is located approximately behind the collarbone (clavicle). The base of the lung reaches as low as the lowest rib, under the chest.

As mentioned previously, the right and left lungs are not identical to each other. The right lung is slightly larger than the left. The left lung must be smaller in order to take room for the heart. The lungs are broken into smaller functional units called lobes. The right lung has three main lobes, and the left lung has two. Every lobe is composed in turn, by lobules: primary, the anatomical units of the lungs, and secondary, which can vary in shape and size. Each secondary lobule is composed of several primary lobules.

Moreover, each lung is located in the pleural sac build up by two membranes called the *pleurae*.

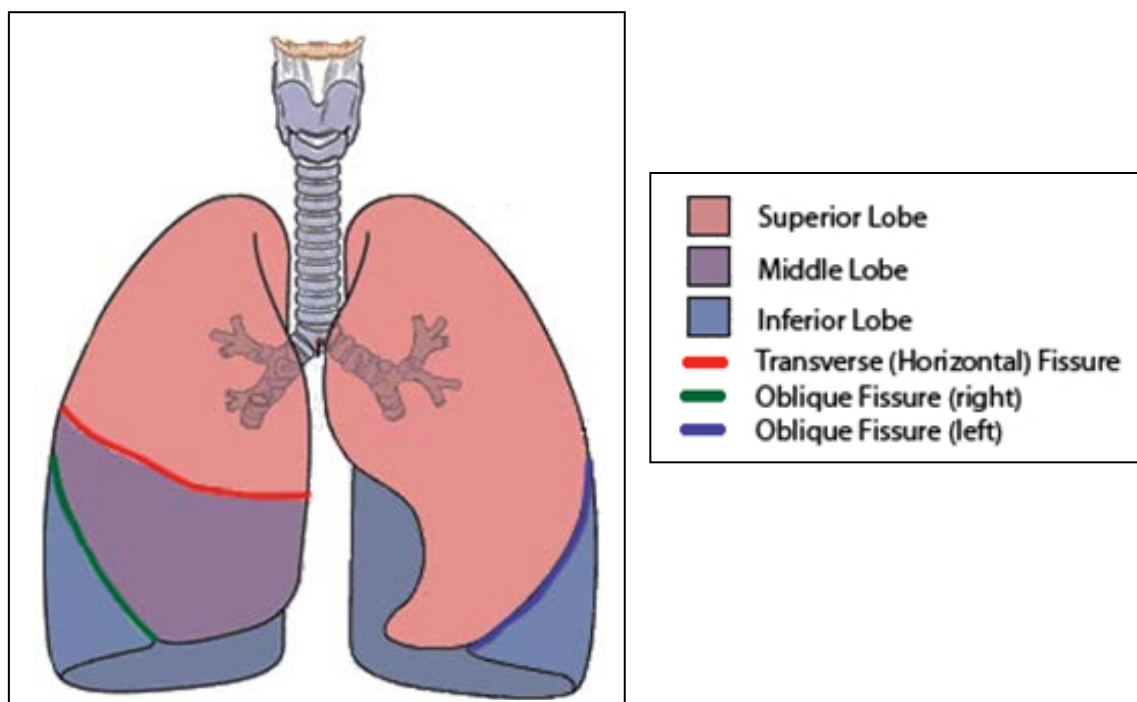


FIGURE I. 5: Fissure and lobes of the lung

Left lung, divided in two lobes by an interlobular fissure and right lung divided into three lobes by two interlobular fissures

Starting in the windpipe, also known as the trachea, the conducting zone then breaks into the two major bronchi (one of which goes to each lung). The bronchi then divide into smaller named bronchi. These named bronchi split in to bronchioli as they go deeper in to the lungs. The bronchioli been divided further to become respiratory bronchioli. These lead directly to alveolar ducts, and then finally to the alveoli.

The alveoli are the microscopic structures where oxygen and carbon dioxide are exchanged into and out of the bloodstream. They are the functional units of the lungs, that is the reason because they have a spherical shape: having a contact surface as big as possible, in order to maximize the gasses exchange. If it were possible to layout the surface area of all the alveoli within the lungs, they would cover approximately 65 to 70 m². That is an area roughly a third the size of a tennis court.

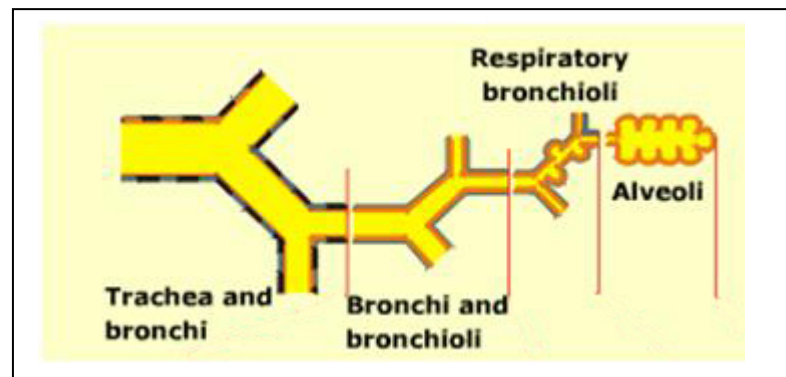


FIGURE I. 6: Bronchial tree scheme

Schematic divisions: Trachea and bronchi, divided in bronchi and bronchioli, respiratory bronchioli then, and alveoli or air sacs at the end.

Lung tissue

Of more interest than the lung's internal structure is the lung tissue as mentioned in our objective. Knowledge of lung tissue can help us choose adequate properties for modeling.

As Henry Gray indicates in (1) *"The substance of the lung is of a light, porous, spongy texture; it floats in water, and crepitates when handled, owing to the presence of air in the alveoli; it is also highly elastic; hence the retracted state of these organs when they are removed from the closed cavity of the thorax. The surface is smooth, shining, and marked out into numerous polyhedral areas, indicating the lobules of the organ"*

The lungs are composed of:

- an external serous coat, or pleura
- a subserous areolar tissue
- the pulmonary substance or parenchyma.

The **pleura** is thin, transparent and covers the entire lung as far as the root. Each lung is covered by an extremely delicate serous membrane that is arranged in the form of a closed sac.

The **subserous areolar tissue** contains a large proportion of elastic fibers; it covers the entire surface of the lung and extends inward between the lobules.

Parenchyma is the whole set of lobules. Inside of the lobules are bronchi, bronchioli and their subdivisions ending in the alveoli. The larger divisions consist of:

- an outer coat of fibrous tissue in which irregular plates of *cartilage* are found in intervals;
- a layer of circular smooth muscle fibers and *smooth muscle* found within the fibrous coat
- the *mucous membrane*, found in the innermost layer, that contains numerous elastic fibers running longitudinally.

The smaller bronchioli differ from the larger tubes: they contain no cartilage. They are about 0.2 mm in diameter. In figure I.7 a sectional representation of a larger airway division is shown.

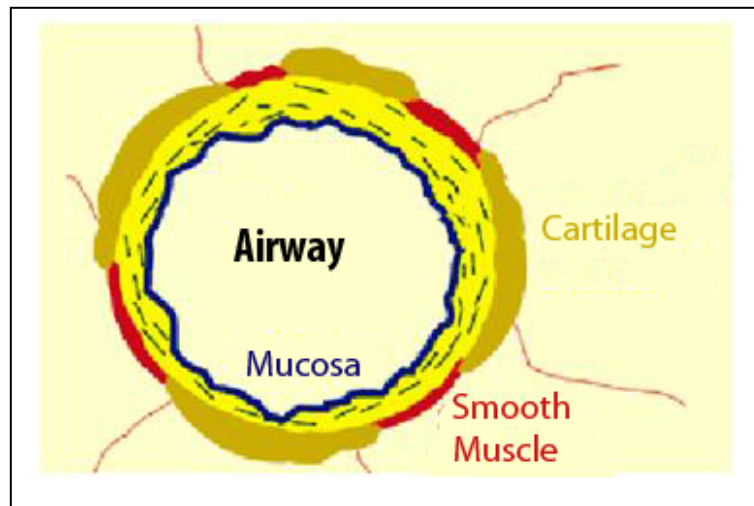


FIGURE I. 7: Internal airways

Sectional cut of the external-most airways. The first structure is cartilage, then there are smooth muscles, and finally there is the mucosa, which seals the airways off from the outside

Further down the bronchioli are the terminal structures called the alveoli. The alveoli are lined by a delicate layer of a simple membrane, the cells of which are joined at their edges by a cementing substance. Outside of the membrane lining is a delicate connective tissue containing numerous elastic fibers and a dense network of blood capillaries forming a common wall to the adjacent alveoli.

It is important to note that after a detailed analysis of lung tissue structure as well as the lining of the bronchial tree, we always find the concept of elastic fibers. This will allow us to allocate our properties model easily be modeled organ, as well as equations well known and certain for our system.

From this point on, lungs would be treated as a homogenous medium, following the recommendations read in the literature. (2)

3.2. Breathing Process

Air moves in and out of the lungs. Breathing is largely an involuntary action controlled by the nervous system.

During breathing, air must first be drawn into the lungs. This process is known as inspiration or inhalation. Following inspiration air must be expelled. This is known as expiration or exhalation.

Inhalation is a process controlled by the brain. Here is how it occurs: Nerve impulses traveling from the brain stimulate the diaphragm, these impulses cause the diaphragm to contract. When it contracts, the diaphragm flattens and lowers. The contraction of the diaphragm draws air into the lungs.

Inhalation also involves the intercostal muscles, the short muscles that lie between the ribs. Nerve impulses traveling to these muscles cause them to contract as the diaphragm is lowered. When the intercostal muscles contract, the rib cage lifts up and out. Together the contractions of the intercostal muscles and the diaphragm increase the volume of the thoracic cavity. This, in turn, decreases the pressure inside the lungs, known as intrapulmonary pressure. As a result, air naturally flows in through the mouth and nose.

In contrast to inhalation, exhalation is a passive process—that is, it does not require muscle contraction in a person at rest. - Exhalation begins after the lungs have filled with air. At this point in the cycle, the diaphragm and the intercostal muscles relax. The relaxed diaphragm rises and resumes its domed shape. The chest wall falls slightly inwards. These changes reduce the volume of the chest cavity. This raises the internal pressure forcing air out.

The lungs also contribute to passive exhalation. During inspiration, the lungs fill like balloons. When inhalation ceases, the elastic fibers inside the lungs cause the lungs to recoil, forcing air out.

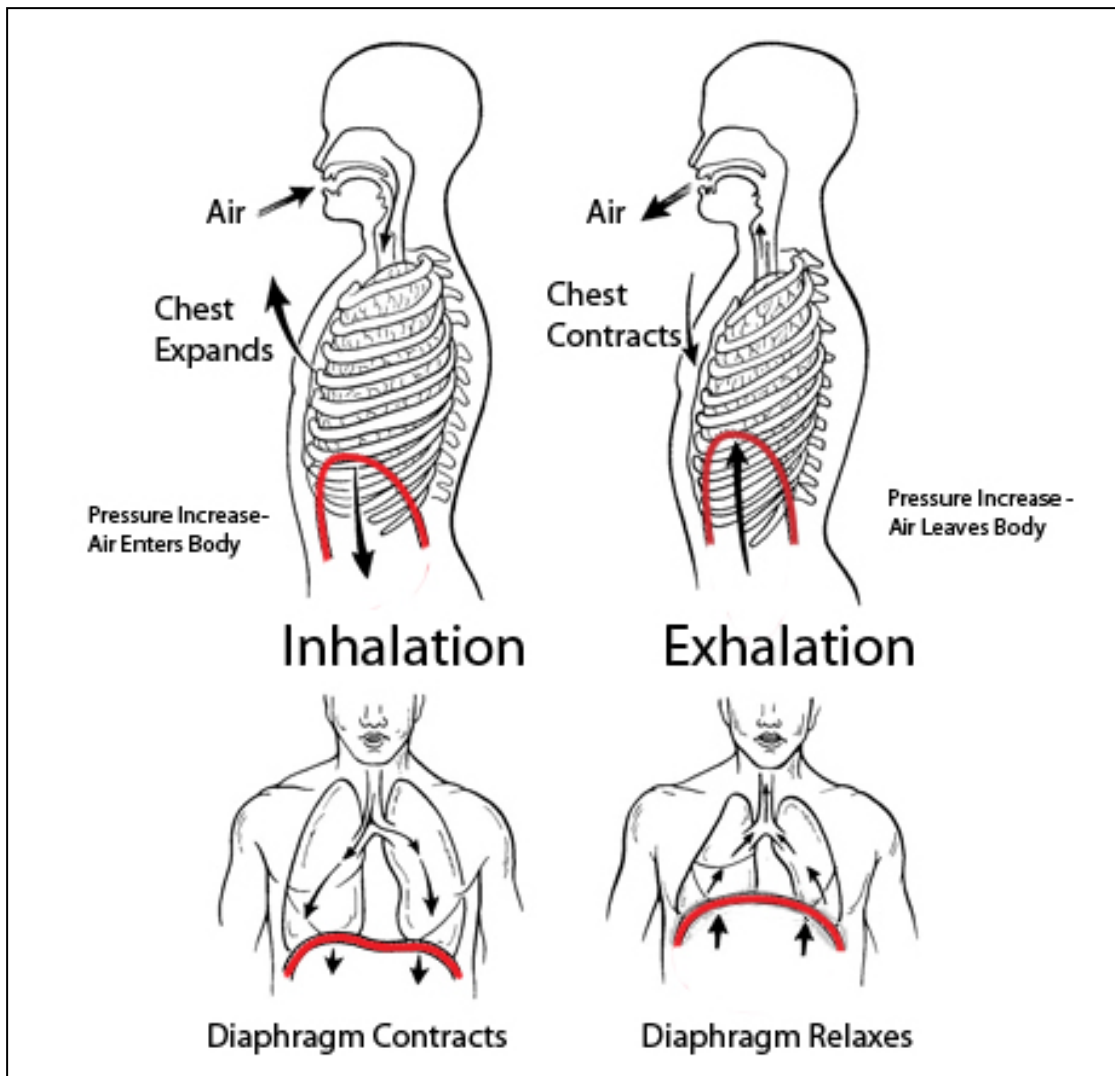


FIGURE I. 8: Inspiration and expiration

Air and muscles' movements during the inspiration and expiration processes.

4. 4D CT

Computed Tomography (CT) plays an important role in radiation therapy. Before defining four-dimensional computed tomography, it is necessary to understand the CT concept.

Equipment:

The CT scanner is typically a large, box like machine with a hole in the center. The patient lies on a narrow examination table that slides in and out of the tunnel. An X-ray tube and electronic X-ray detectors located opposite each other on a ring (called a **gantry**) rotates around the patient. A computer workstation processes the imaging information.

How it works:

In many ways CT scanning works very much like other x-ray examinations. Different body parts absorb the x-rays in varying degrees. In a conventional x-ray exam, a small burst of radiation is aimed at and passes through the body, recording an image on photographic film or a special image recording plate. Bones appear white on the x-ray, soft tissue shows up in shades of gray and air appears black.

In CT scanning, numerous x-ray beams and a set of electronic x-ray detectors rotate around the patient, measuring the amount of radiation being absorbed throughout the body. Simultaneously, the examination table is moving through the scanner, so that the x-ray beam follows a spiral path. The specific software creates two-dimensional cross-sectional images of its body (axial plane). This technique is called helical or spiral CT and is currently one of the most prolific methods in use.

CT images are like a stack of thin slices. When the image slices are reassembled by computer software, the result is a very detailed multidimensional view of the body's interior. Refinements in detector technology allow new CT scanners to obtain multiple slices in a single rotation. These scanners, called **multi-slice CT** allow thinner slices to be obtained in a shorter period of time, resulting in more detail and additional view capabilities.

Any motion during scanning (either breathing or body movements), can lead to artifacts on the images. Artifacts will be treated later in this document, but in brief, artifacts give a low spatial resolution in the images which can appear as blurring zones.

4D CT:

4D CT describes a 3D image that is imbued with a fourth dimension, time. In this case, 4D CT is capable of generating images that are correlated with a patient's respiratory cycle over a period of time. These image data sets are very useful to determinate normal organ motion.

The technique for 4D CT is very similar to 3D CT. The image acquisition is performed in **Cine Mode**, which the gantry rotates multiple times at the same table position, while several scans are taken, for different time frames. When a patient has completed one respiratory cycle, the table is then incremented to an adjacent location and another cine scan series is acquired. This is repeated for the length of the anatomy being scanned.

Scan time at each position is recommended by the scanner's manufacturer to be at least as long as the period of the respiratory cycle plus one rotation. For example, if the patient is breathing at a rate of 15 breaths per minute, the duration of one respiratory cycle is 4 seconds. If the scanner is operated at a rotation speed of 0.5 seconds per rotation, cine mode image data should be acquired at each bed location for 4.5 seconds. The number of cine scans (table positions) is determined by the user, based on the length of the volume to cover.

The result is a set of cine CT images at multiple phases throughout the respiratory cycle. Every cine CT images are encoded with the respiratory waveform. The images are then transferred to a workstation with a 4D application. The 4D application correlates the CT images with the respiratory waveform and displays a movie loop of respiratory phases over the entire range of anatomy scanned. The number of phases is user-defined; commonly this number is fixed at 10.

PART II:

LUNG MODEL

The main aspects of the process of lung ventilation are identified and outlined as the starting point to model the respiratory motion. The model basically consists of lung volume enclosed by a compartment. Using this idea, we simulate the process of lung ventilation by applying prescribed pressures at the surface of the lung. Lung expansion is limited by a second geometry representing the walls of the chest cavity. Penetration of the lung into the chest cavity's walls is avoided. As an approved method in biophysical modeling, Finite Element Methods (FEM) are applied using the software ABAQUS. (Abaqus 6.10-EF2). In the next section, the model used to describe the elastic behavior of the lung is described.

1. MODEL EQUATIONS

The starting point of the modeling is the process of **lung ventilation**. It has been already discussed in previous sections, but its main aspects and several new ideas would be described shortly.

The lungs themselves are not actively moving. Each lung is located in the pleural sac built up by two membranes called the *pleurae*. Outer pleura (parietal pleura) is adherent to the internal surface of the thoracic cavity and the diaphragm. The inner pleura (visceral pleura) covers the lung and is adherent to its surface. Parietal and visceral pleura are joined together at the root of the lung. The space enclosed is known as the *pleural cavity*. It is subject to a negative pressure (the intrapleural pressure) and filled with a fluid. Due to the negative pressure the pleurae are in close contact. The contact is frictionless due to the fluid within the pleural cavity.

During breathing the thoracic cavity is expanded by contraction of the diaphragm and outer intercostal muscles. This causes changes in the intrapleural pressure which acts as a

force upon the lung surface. Hence lung expands, and during this process the visceral pleura slides frictionlessly down the internal surface of the thoracic cavity.

This process is modeled as a contact problem in the framework of the theory of elasticity. A uniform negative pressure (intrapleural pressure) is applied to a lung representing the initial state of breathing.

As initial state of breathing, we choose the state in which one of the lungs has its minimum volume. This state is known as End of Expiration state (EE onwards). The final state is the moment when the lung volume reaches its maximum. It is End of Inhalation state. (EI)

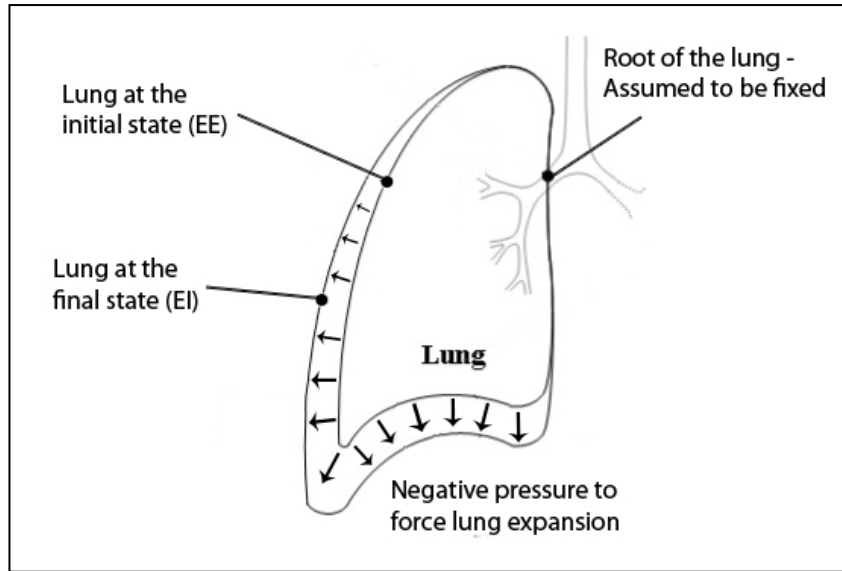


FIGURE II. 1: Principle and terminology

At the EE state, the negative pressure applied causes the lung to expand. The expansion is limited by a geometry representing the lung shape at EI state.

We aim at a state in which the initial lung geometry deformed by the intrapleural pressure nearly matches the limiting geometry. This state should be an equilibrium state; i. e. external forces should be balanced out by the inner lung's reacting forces specified by the Cauchy stress tensor, σ .

Given equilibrium, the corresponding deformation field $\mathbf{u} : \mathbb{R}^3 \rightarrow \mathbb{R}^3$ is sought. \mathbf{u} is interpreted to be an estimation of the inner lung motion field during breathing, where our assumption is that breathing is the responsible for the change from EE to EI. As no volume forces are considered, equilibrium is characterized by:

$$\text{div } \sigma = 0 \quad (\text{Eq.II.1})$$

Lung tissue is assumed to obey Hooke's law, i.e., the components of the stress tensor, σ_{ij} , are linearly proportional to the components of the strain tensor, ε_{kl} ; with a constant, C_{ijkl} :

$$\sigma_{ij} = C_{ijkl} \cdot \varepsilon_{kl} \quad (\text{Eq.II.2})$$

In an anisotropic linear elastic and homogeneous medium, the number of elastic constants C_{ijkl} obtained is reduced to two. Writing out the previous equation for this particular material in Cartesian coordinates:

$$\sigma_x = \lambda \cdot (\varepsilon_x + \varepsilon_y + \varepsilon_z) + 2 \cdot \mu \cdot \varepsilon_x \quad (\text{Eq.II.3})$$

$$\sigma_y = \lambda \cdot (\varepsilon_x + \varepsilon_y + \varepsilon_z) + 2 \cdot \mu \cdot \varepsilon_y \quad (\text{Eq.II.4})$$

$$\sigma_z = \lambda \cdot (\varepsilon_x + \varepsilon_y + \varepsilon_z) + 2 \cdot \mu \cdot \varepsilon_z \quad (\text{Eq.II.5})$$

$$\sigma_{xy} = 2 \cdot \mu \cdot \varepsilon_{xy} \quad (\text{Eq.II.6})$$

$$\sigma_{yz} = 2 \cdot \mu \cdot \varepsilon_{yz} \quad (\text{Eq.II.7})$$

$$\sigma_{xz} = 2 \cdot \mu \cdot \varepsilon_{xz} \quad (\text{Eq.II.8})$$

Where λ and μ are called the *Lamé Constants*. In the engineering literature the second Lamé constant, μ ; is commonly written as G , and is called *shear modulus*.

Customarily, these equations appear in the inverted form:

$$\varepsilon_x = \frac{1}{E} [\sigma_x - \nu(\sigma_y + \sigma_z)] \quad (\text{Eq.II.9})$$

$$\varepsilon_y = \frac{1}{E} [\sigma_y - \nu(\sigma_x + \sigma_z)] \quad (\text{Eq.II.10})$$

$$\varepsilon_z = \frac{1}{E} [\sigma_z - \nu(\sigma_x + \sigma_y)] \quad (\text{Eq.II.11})$$

$$\varepsilon_{xy} = \frac{1+\nu}{E} \sigma_{xy} = \frac{1}{2G} \sigma_{xy} \quad (\text{Eq.II.12})$$

$$\varepsilon_{xz} = \frac{1+\nu}{E} \sigma_{xz} = \frac{1}{2G} \sigma_{xz} \quad (\text{Eq.II.13})$$

$$\varepsilon_{yz} = \frac{1+\nu}{E} \sigma_{yz} = \frac{1}{2G} \sigma_{yz} \quad (\text{Eq.II.14})$$

Where E is the Young's modulus and ν the Poisson's ratio. Both constants will be discussed later.

Equations (Eq. II.3) to (Eq. II.8) can be written in a matrix form:

$$[\sigma] = [C(E, \nu)] \cdot [\varepsilon] \quad (\text{Eq.II.15})$$

Lung volume changes are in the order of 20 % of the lung volume at EE within a breathing cycle, i. e. large deformations are expected to occur; therefore Green-Lagrange strain tensor is used which enables for large deformation analysis.

$$\varepsilon = \frac{1}{2} \cdot (\nabla \mathbf{u} + \nabla \mathbf{u}^T + \nabla \mathbf{u}^T \nabla \mathbf{u}) \quad (\text{Eq.II.16})$$

Equations (Eq.II.1), (Eq.II.15) and (Eq.II.16) form the governing equations of the problem to be solved. The problem specification is completed with the **boundary conditions**.

Boundary Conditions:

No displacements are allowed at the root of the lung, and the limiting geometry is also fixed:

$$\mathbf{u} = 0 \quad (\text{Eq.II.17})$$

for the root of the lung and the limiting geometry.

No penetration of deformed initial lung geometry into the limiting geometry should occur. This poses a contact problem. Here contact is frictionless due to the fluid within the pleural cavity, which yields additional boundary conditions to be fulfilled at the deformed initial geometry surface.

In case of contact between deformed the initial lung geometry surface and the limiting geometry, surface penetration is prevented by introducing contact forces. Contact forces are represented as a contact pressure: $p_{contact}$.

$$g \geq 0 \quad (\text{Eq.II.18})$$

$$p_{contact} \leq 0 \quad (\text{Eq.II.19})$$

$$g \cdot p_{contact} = 0 \quad (\text{Eq.II.20})$$

Where g denotes the normal gap distance, i. e. the distance between the deformed initial geometry surface and the limiting geometry surface. This new variable to define 3 scenarios:

$g > 0$: Separation,

$g = 0$: Contact,

$g < 0$: Penetration,

Contact forces are represented by $p_{contact} \mathbf{n}$ with \mathbf{n} the normal vector pointing outwards the deformed lung surface.

Contact pressure and intrapleural pressure together define the stress boundary conditions:

$$\sigma \mathbf{n} = (p_{contact} + p_{intrapl}) \mathbf{n} \quad (\text{Eq.II.21})$$

$p_{intrapl} \geq 0$: intrapleural pressure.

Equations (Eq.II.17) to (Eq.II.21) represent the boundary conditions for the problem to be considered.

2. FINITE ELEMENT METHODS

After defining the equations model and the boundary conditions, we proceed to solve it. As an approved method in biophysical modeling, Finite elements are applied using specific software for this purpose. This section reviews the basic idea of FE, and the main aspects that solve our system.

We will use a very simplified model, which represent the characteristics of our system has, but led it to one-dimensional case, thereby is serving to explain the finite element method, without going into the complexity that would result 3 dimensions.

The idea is based on an encastred beam, under a horizontal force. The beam represents the lung, encastred the fixed points at the root of it, and the horizontal force corresponding to the pressure applied to the outer surface to achieve the desired displacement. As there is no force in the vertical direction, there are no efforts or movement therefore, in that direction. It is then a one-dimensional problem, in which the goal is simply to obtain the displacement at each point of the beam. Figure II.2 shows a diagram of the system.

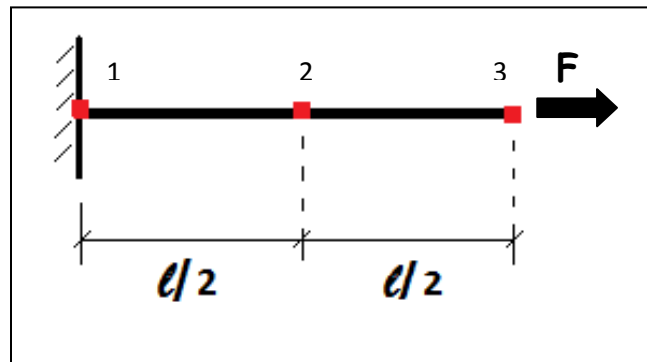


FIGURE II. 2: Encastred Beam

The beam is of length l is defined by 3 nodes, resulting in a total of 2 elements, as shown in Figure II.2.

Shape Functions

The first step in any finite elements problem is to compute the shape functions. The shape or influence functions are relative to each node and define the displacement field within each element from the displacements of the nodes. They are interpolation functions within the interior of the element. The relationship between \mathbf{a} (displacements in the nodes-discrete-), \mathbf{N} (shape functions), and \mathbf{u} (displacement-continuous-) is as follows:

$$\mathbf{u} = \mathbf{N}\mathbf{a} \quad (\text{Eq.II.22})$$

The shape functions are square matrices of size 1x1, 2x2 or 3x3 depending on the size of the problem.

In addition, next conditions must be met:

$$N_i = 1 \text{ at the node } i$$

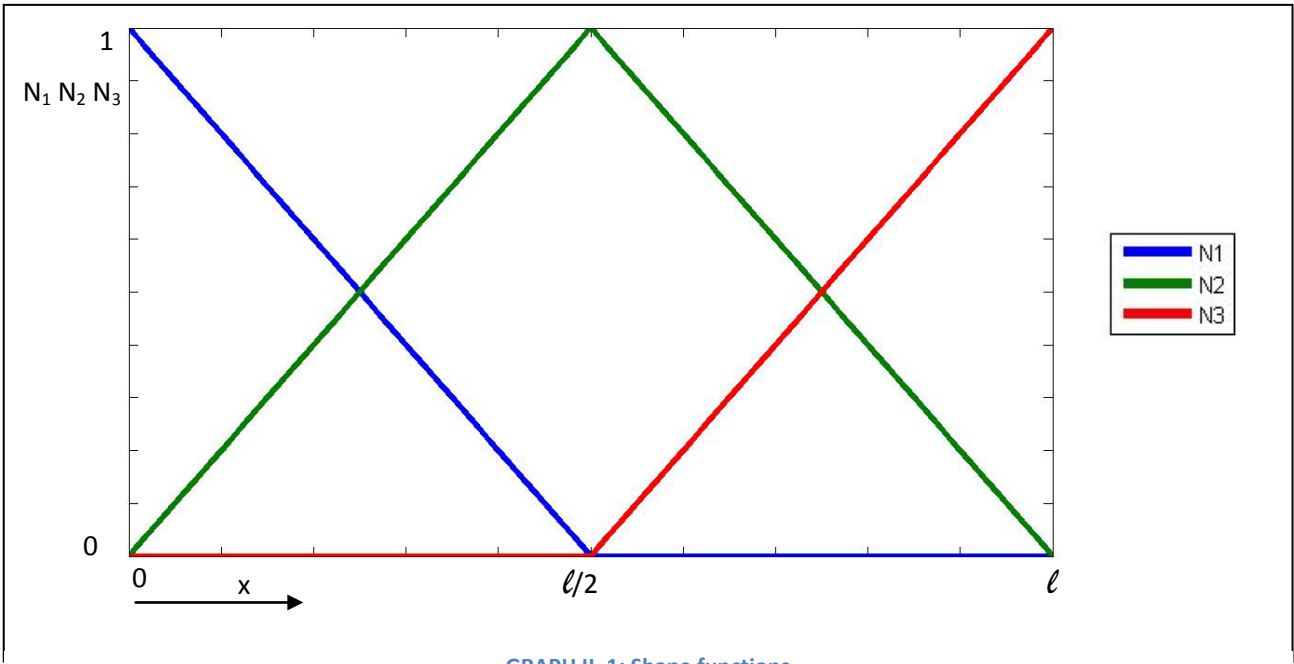
$$N_i = 0 \text{ at other nodes}$$

In our 3 nodes-one-dimensional example:

$$\mathbf{a} = \begin{bmatrix} a_1 \\ a_2 \\ a_3 \end{bmatrix} = \begin{bmatrix} u_{1x} \\ u_{2x} \\ u_{3x} \end{bmatrix} \quad (\text{Eq.II.23})$$

$$\mathbf{N} = [N_1 | N_2 | N_3] \quad (\text{Eq.II.24})$$

We implement linear shape functions, as shown in the chart below, for easy deployment.



According to this graph, it is easy obtaining equations governing the shape functions:

$$N_1 = \begin{cases} 1 - \frac{2x}{l} & \text{if } x \leq l/2 \\ 0 & \text{other case} \end{cases} \quad (\text{Eq.II.25})$$

$$N_2 = \begin{cases} \frac{2x}{l} & \text{if } x \leq l/2 \\ 1 - \frac{2(x - \frac{l}{2})}{l} & \text{if } x \geq l/2 \end{cases} \quad (\text{Eq.II.26})$$

$$N_3 = \begin{cases} 0 & \text{other case} \\ \frac{2(x - \frac{l}{2})}{l} & \text{if } x \geq l/2 \end{cases} \quad (\text{Eq.II.27})$$

Deformations

The displacements vector at the nodes is related to the strain vector ε , through the matrix B, which contains the partial derivatives of shape functions.

For a generic case with large displacement, the relationship between epsilon and the displacement field is:

$$\varepsilon = \frac{1}{2} [\nabla u + \nabla u^T + \nabla u \nabla u^T] \quad (\text{Eq.II.28})$$

In our case, being one-dimensional:

$$\nabla u = \nabla u^T = \frac{\partial u}{\partial x} \quad (\text{Eq.II.29})$$

Using shape functions:

$$\frac{\partial u}{\partial x} = \frac{\partial N}{\partial x} \cdot a \quad (\text{Eq.II.30})$$

$$\varepsilon = \frac{1}{2} \left[2 \cdot \frac{\partial N}{\partial x} \cdot a + \left(\frac{\partial N}{\partial x} \cdot a \right)^2 \right] = \frac{\partial N}{\partial x} \cdot a + \frac{1}{2} \left(\frac{\partial N}{\partial x} \cdot a \right)^2 \quad (\text{Eq.II.31})$$

The matrix of partial derivatives in the one dimensional case we are dealing with is of dimensions 1x1, and equal to

$$B = \frac{\partial N}{\partial x} \quad (\text{Eq.II.32})$$

The final expression for ε is finally:

$$\varepsilon = Ba + \frac{1}{2}B^2a^2 \quad (\text{Eq.II.33})$$

As can be seen, there is a nonlinear term because we are considering large displacements. To simplify the calculation described in this chapter, we assume small displacements. Therefore, the above expression can be simplified by the following:

$$\varepsilon \approx Ba \quad (\text{Eq.II.34})$$

Constitutive Equation:

The relationship between stress and strain can be deduced from the equation of linear elasticity.

$$\sigma = D \cdot \varepsilon \quad (\text{Eq.II.35})$$

In this case, being one-dimensional case, the matrix of elastic constants D , has dimension 1x1 and is equal to the elastic modulus of the material E . In one three-dimensional case with an isotropic material, D only depends on two independent variables, and has dimensions of 6x6.

Integral equation of equilibrium: The principle of virtual works:

From the relations between displacements, stresses and strains, the mathematical problem is formulated as a balance between the work done by internal forces at each node and the stored elastic deformation force in the solid.

Let p be the vector of loads applied to nodes.

$$\mathbf{p} = \begin{bmatrix} p_1 \\ p_2 \\ p_3 \end{bmatrix} \quad (\text{Eq.II.36})$$

$$\sum_i p_i a_i = \int \sigma \cdot \varepsilon dv = \int (D \cdot \varepsilon) \varepsilon dv = \int (DBa)^T (Ba) dv = a^T \left(\int B^T D B dv \right) a \quad (\text{Eq.II.37})$$

$$\sum_i p_i a_i = a^T \left(D \cdot \int B^T B dv \right) a \quad (\text{Eq.II.38})$$

Equating terms and simplifying:

$$p^T = a^T \left(D \cdot \int B^T B dv \right) \quad (\text{Eq.II.39})$$

We define the stiffness matrix K as the matrix that relates the nodes loads and its displacements.

$$K = D \cdot \int B^T B dv \quad (\text{Eq.II.40})$$

In our one-dimensional example, the matrix K has dimensions 3×3 because there are 3 nodes, and dv is actually dx , which greatly simplifies the problem.

If we transpose the equation Eq.II.39, we obtain a simpler notation:

$$p = Ka \quad (\text{Eq.II.41})$$

Developing the above equation we obtain the following algebraic equations:

$$p_1 = a_1 k_{11} + a_2 k_{12} + a_3 k_{13} \quad (\text{Eq.II.42})$$

$$p_2 = a_1 k_{21} + a_2 k_{22} + a_3 k_{23} \quad (\text{Eq.II.43})$$

$$p_3 = a_1 k_{31} + a_2 k_{32} + a_3 k_{33} \quad (\text{Eq.II.44})$$

Then we apply the boundary conditions, which is to replace known data.

- From node 1, we know that their displacement is zero, because it is encastred, but do not know the load applied (reaction)
- From node 2, we know there is no load applied, but the displacement is unknown.
- From node 3, we know the applied load, $p_3 = F / A$, but displacement is also unknown.

With this information, we can solve the unknown variables p_1 , a_2 , a_3 , in the previous system.

$$-p_1 + a_2 k_{12} + a_3 k_{13} = -a_1 k_{11} \quad (\text{Eq.II.45})$$

$$a_2 k_{22} + a_3 k_{23} = p_2 - a_1 k_{21} \quad (\text{Eq.II.46})$$

$$a_2 k_{32} + a_3 k_{33} = p_3 - a_1 k_{31} \quad (\text{Eq.II.47})$$

The system to be solved in matrix form is therefore as follows:

$$\begin{bmatrix} -1 & k_{12} & k_{13} \\ 0 & k_{22} & k_{23} \\ 0 & k_{32} & k_{33} \end{bmatrix} \cdot \begin{bmatrix} p_1 \\ a_2 \\ a_3 \end{bmatrix} = \begin{bmatrix} -a_1 k_{11} \\ p_2 - a_1 k_{21} \\ p_3 - a_1 k_{31} \end{bmatrix} \quad (\text{Eq.II.48})$$

The resulting system $Ax = b$, is the corresponding system of linear equations that the software solves. This is invert the matrix A , and obtain the vector x . Thus all displacements are

determined at the nodes, a_i . With the shape functions N_i , the displacements at any point of the solid are determined.

Up to now is the one-dimensional example. The case in three dimensions is much more complicated, since it is a problem with nonlinear terms, and cannot assume the simplification of $\varepsilon \approx Ba$. Moreover, the system of algebraic equations to solve is much more complex, due to the large size of the matrix A .

This method is only intended to show the technique of finite elements, and not the algebraic details, so many simplifications have been assumed that in the real case are not taken into account.

3. OBTAINING DATA

4D data sets open up the possibility to measure breathing motion of inner organs. Depending on image quality and resolution, they enable the verification of respiratory motion modeling approaches. In this study we use spatially and temporally high resolved 4D CT image data of a lung tumor patient. The patient was examined with a 4-slice GE LightSpeed CT scanner (GE Medical Systems, Milwaukee, WI, USA). The scanner was operated in the axial cine mode. The gantry speed was set to be 1 rotation per second. The cine duration was set to be the average observed breathing period of the patient plus an additional second to account for variations in the breathing period. Depending on the respiratory period for each patient, a different number of axial CT slices (usually ranging from 11 to 20) were reconstructed from the x-ray projections at each couch position. Each CT slice has a thickness of 2.5 mm, so each scan at one couch position covers 1 cm of the patient body in the superior–inferior (SI) direction.

The resulting spatiotemporal data set is a series of CT scans, each scan covering a part of the thorax for a given breathing phase; were used to reconstruct 4D CT data images representing a series of 3D CT images for a scale of user-defined breathing phases. The temporal resolution was fixed at 10 breathing phases, sampled equidistantly over the breathing cycle.

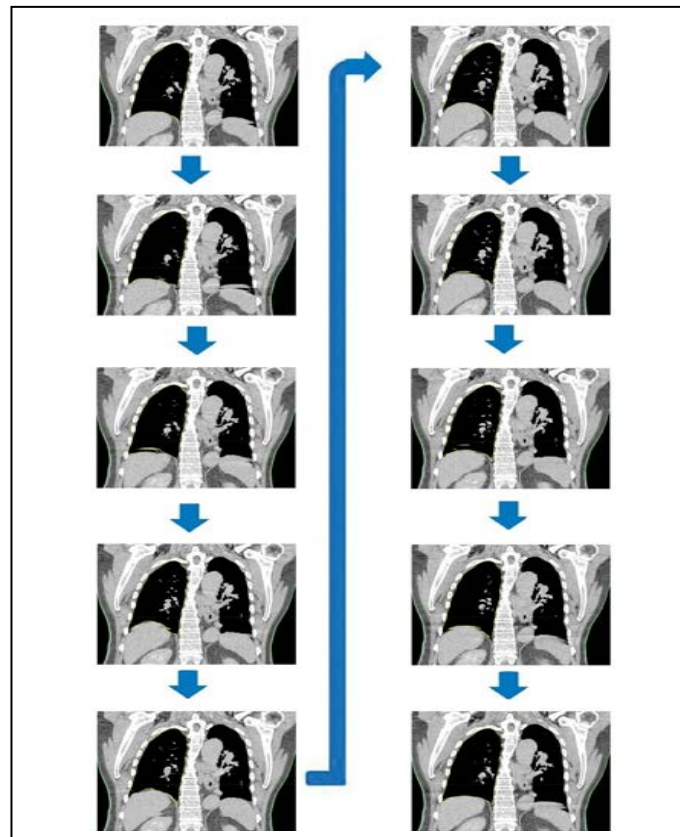


FIGURE II. 3: 4D CT 10 breathing phases

10 frontal images of the 10 phases of respiration in 4D-CT

Once the 4D CT images were taken, these were imported to clinical software ECLIPSE (Varian Inc) which was automatically detected the lungs' contour slice by slice in each one of the 10 breathing phases. Cause to the lungs are full of air, is easily appreciated the gray level difference in them. ECLIPSE lets contours automatic detection only changing threshold gray levels.

All contours were reviewed by a medical physics expert to check the lung's contours are equally detected in all phases.

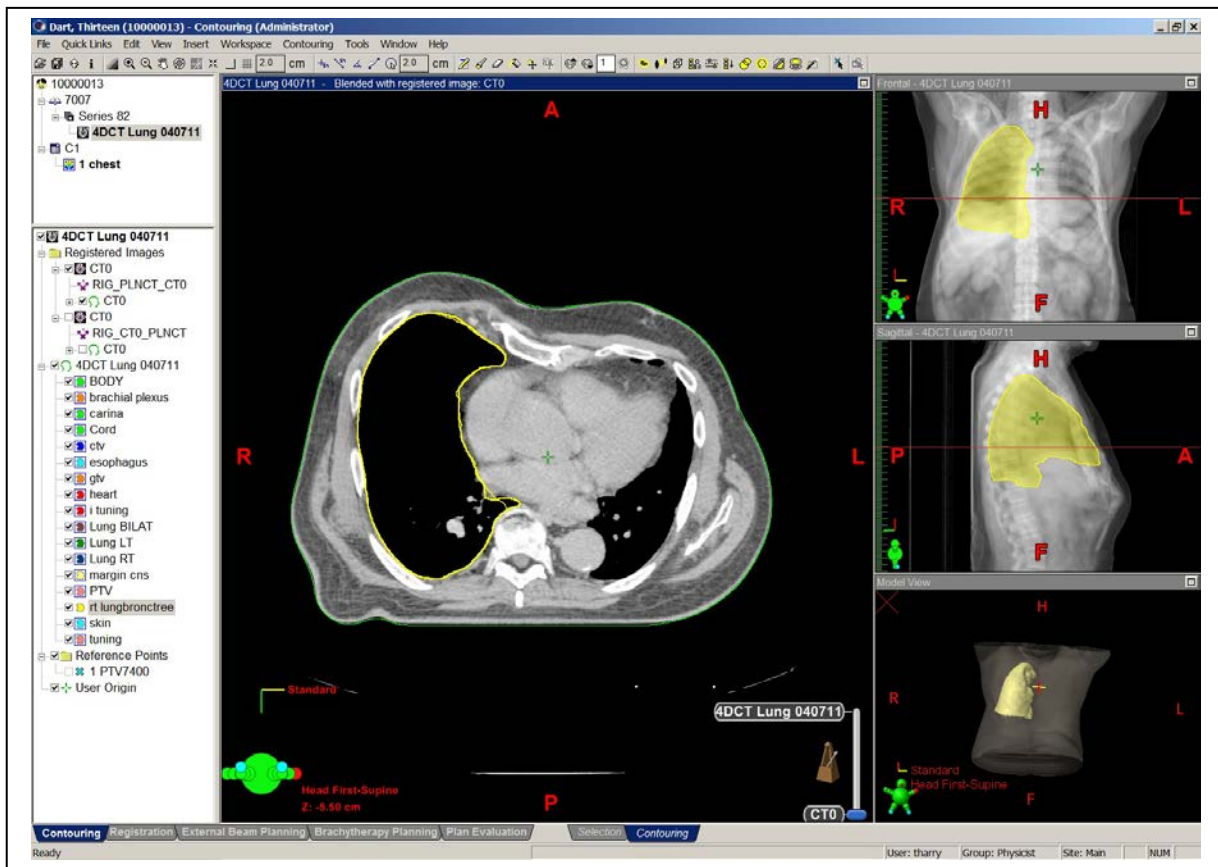


FIGURE II. 4: ECLIPSE snapshot

3 cut view are represented in ECLIPSE's main window: axial, in the left side; frontal, on the right top side, and sagital, in right side in the center.

From this point, in order to optimize the data storage and the computational time, the entire model developing will be based on a single lung. In this case, we choose the right lung, because its shape is the bigger one by the absence of heart.

Once the contours are selected, two types of files are exported from ECLIPSE and imported into MATLAB (MATLABR2010b) for each breathing phase. The first file contains information about the 4D CT as well as the patient. The second file stores information about the

points coordinates (x, y) forming the boundary of the region of interest (ROI) in each one of the slices. Both are type dicom files (. dcm).

In MATLAB we proceed to the extraction of the contours through the internal program function *poly2mask*. The result is a binary three dimensional matrix for every phase.

In the next chapters, the steps for the lung final geometry generation will be explained. In deep.

4. MESH GENERATION

4.1. Overview

In a finite elements problem an important point is the mesh. The finite elements are joined by shared nodes and the collection of nodes and finite elements are called the mesh. Thus the mesh is going to be the “stage” where we are solving our numerical problem.

There are multiple mesh configurations but the most used are triangular and rectangular in 2 dimensions, and tetrahedral and hexahedral in 3 dimensions, typically. In this section we focus on the mesh used in this project, that of the lung geometry.

Due to the complex shape we are working with, the best way to fit the real shape into a mesh is with triangular elements. As a first step in the mesh generation, we extract a 3D surface meshed with triangular elements. Later, the bi-dimensional surface will be converted into a tridimensional meshed volume, from the triangles forming the surface.

Several algorithms exist in medical imaging mesh generation. Particularly, the meshing algorithm we are working with is based on **Delaunay triangulation**.

The Delaunay triangulation is a triangulation method widely used in mesh generation. This is one of the fastest triangulation methods and relatively easy to implement, giving excellent results for most applications. It involves the generation of points on the domain and their connection to form a triangulation, which satisfies some optimality conditions.

The main idea of the triangulation method will be explained in 2 dimensions, and then, the result will be extrapolated in a 3 dimensional case.

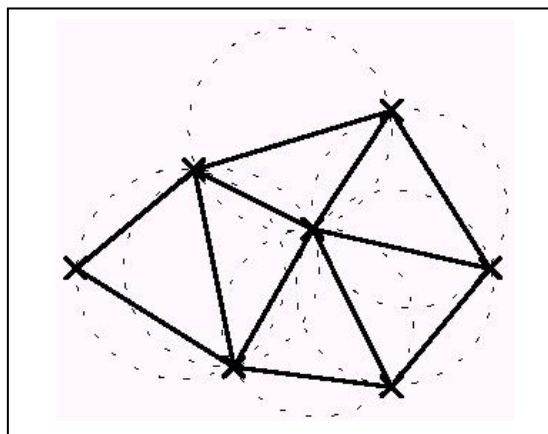


FIGURE II. 5: Delaunay triangulation

In figure II.5 we can see a 2 dimensional Delaunay triangulation. To become a Delaunay triangulation, a set of points $P = \{p_1, p_2, \dots, p_n\}$ has to satisfy a property called “**empty circle property**” or “**Delaunay’s criterion**”:

“If a circle is drawn using the vertexes of any triangle in Delaunay triangulation, the circle shouldn’t contain any other point of the set”.

In figure II.6, the later property is shown schematically. Figure II.6 a) doesn’t agree with Delaunay’s criterion because when the circle passing across the three vertex p_1 , p_2 , and p_3 of the element T_a , a point, p_4 , results inside the circle. By contrast, figure II.6 b) is agreed with Delaunay’s criterion, because both circles passing through the 3 vertexes of every triangle are “empty” of points, i.e. the circles don’t enclose any point within their areas.

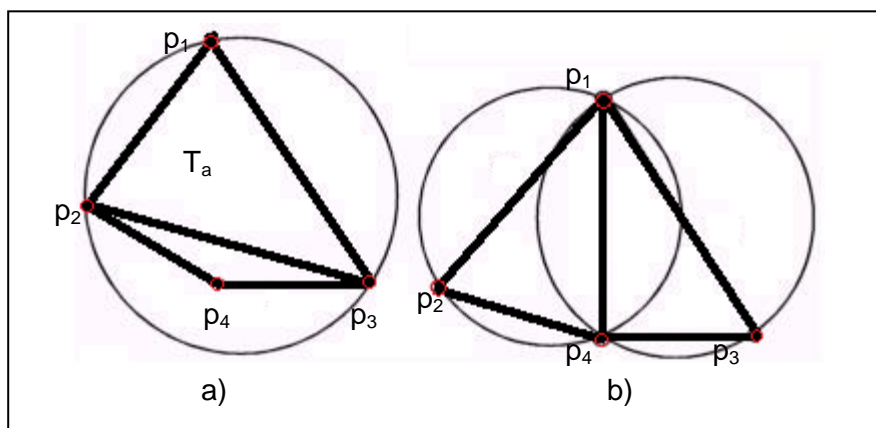


FIGURE II. 6: Delaunay’s criterion

a) Doesn’t agree with Delaunay’s criterion

b) Agree with Delaunay’s criterion

When Delaunay’s criterion is not fulfilled, it is said to exist an “**illegal edge**”. Figure II.6 a) doesn’t agree with Delaunay’s triangulation, that is: the triangle T_a contains an illegal edge shared with the adjacent triangle, which contains the point p_4 .

“Flip” or “edge legalization”:

To guarantee empty circle property, triangles with “illegal” edges are checked. Then, the illegal edge is subject from the process called “flip” or “edge legalized”. This process consists of converting the illegal edge in a legal one. Figure II.7 represents how an edge can flip.

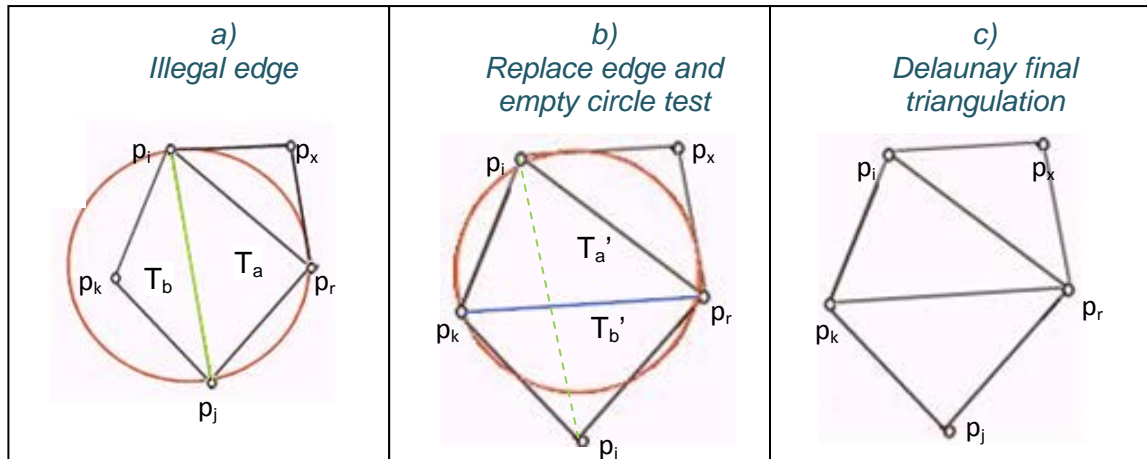


FIGURE II. 8: Flipping edge

Figure II.7 in a) the circle passing across the three vertexes of T_a , encloses point p_2 , thus between triangles T_a and T_b an illegal edge exists (in green). To correct this problem, the illegal edge has to be “flipped”. Figure II.7.b) shows this procedure: The illegal edge (green dashed line), has been replaced by a legal edge (in blue). The new triangles T'_a and T'_b fulfill the criterion as shown the red circle. In figure II.7. c) the final triangulation can be seen.

Delaunay triangulation algorithm:

To carry out Delaunay triangulation, we begin with a triangle p_1, p_2, p_3 ; which is big enough to enclose all the points in the set P . This triangle, is used as initial and auxiliary triangle, and at the end, all the edges from p_1, p_2 and p_3 will be dismissed.

Step 1: Create the initial triangulation T , with the points p_1, p_2 and p_3 . All points in the set P have to be contained in the triangle T . The right side in the figure II.8 shows this step.

Step 2: Points in the set P , will be inserted in the triangulation in the same order they were generated. If p_r is the new inserted point, 3 edges are added, from p_r to the 3 vertexes of the outer triangle to p_r . as shown left side of the figure below. The result is 3 new triangles. The new edges (marked in blue) have to be checked if they agree with Delaunay’s criterion. If they agree, a new point is inserted within each new triangle. If the criterion is not fulfilled, then the subroutine **legalize_edge** is called.

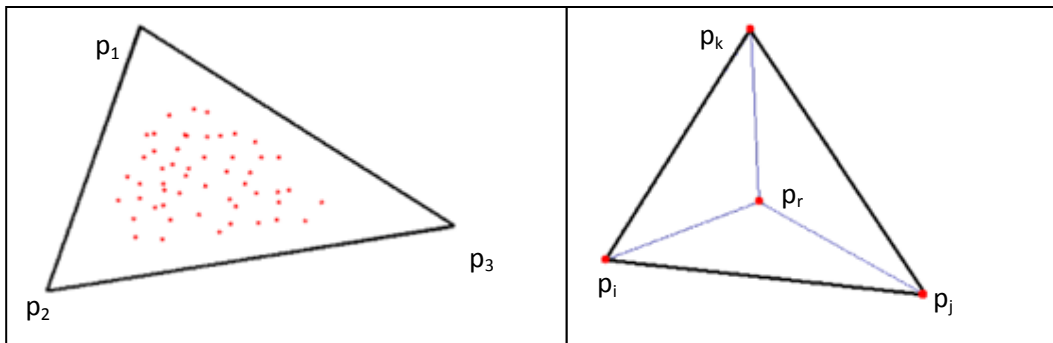


FIGURE II. 9: Steps 1 and 2 in Delaunay algorithm

Legalize_edge (p_r, p_i, p_j, T)

- The new inserted point is p_r , and $p_i p_j$ is the edge that may need to be flipped, as shown figure II.7 a).
- Delaunay property is checked, generating the circle passing across the points p_r, p_i and p_j . If any point p_k exists in the interior of the circle, then the edge $p_i p_j$ is illegal.
- When an edge $p_i p_j$ is illegal, an adjacent triangle $p_i p_j p_k$ exists, sharing the edge $p_i p_j$ with the triangle $p_r p_i p_j$. In order to avoid the illegality of the edge $p_i p_j$, it is flipped, replacing $p_i p_j$ by $p_r p_k$. This procedure is shown in figure II.7.b).

Furthermore, a property of Delaunay triangulation that hasn't been mentioned yet is that this triangulation owns the biggest angles vector between all possible triangulations. "Angles vector" is referring to the angles created by the triangulation edges. In a Delaunay triangulation, they would be those angles bigger or equal than in any other triangulation method. This property about the angles makes Delaunay's method as one of the most used in finite elements meshes, and that is because the maximum area in every element is guaranteed, or the closest to the equilateral shape.

Up to here is the bi-dimensional explanation of Delaunay's algorithm. Based on this idea, we can apply this procedure in 3 dimensions too. This is a more complex process, and it falls outside the scope of this project. References (3), (4) and (5) contain a deeper explanation about the algorithm extrapolated to the three-dimensional case.

4.2. Implementation

Mesh generation is a difficult task to implement manually. There are several free opened-sourced software well elaborated that can cover this problem easily.

To generate the lung 3D mesh we used the toolbox *iso2mesh*. (See Appendix A).

Iso2mesh consists of a wide range of functions, but for mesh generation only is necessary to use one. The function to use is called *vol2surf* and its principal inputs, outputs as well as the main basis of the mesh generation algorithm will be described.

Inputs:

- Volumetric binary image
- Maximum radius of the circumference outside each triangle in the resulting meshing

Outputs:

- list of nodes on the resulting surface mesh
- List of triangular elements on the resulting surface

The meshing algorithm is based on Delaunay refinement explained before.

To evaluate the mesh quality generated, two mesh parameters are computed: *shape factor* (SF) and *aspect ratio* (AR). In this case both are given by the finite elements software ABAQUS, but similar software could have been used for this purpose. Even these parameters could have been easily computed by the user.

Shape factor

ABAQUS/CAE highlights elements with a normalized shape factor smaller than a specified value. The shape factor ranges from 0 to 1, with 1 indicating the optimal element shape and 0 indicating a degenerate element. The normalized shape factor is defined as:

$$SF = \text{shape factor} = \frac{\text{element area}}{\text{optimal element area}} \quad (\text{Eq.II.49})$$

Optimal element area is the area of an equilateral triangle with the same circumradius as the element. (The circumradius is the radius of the circle passing through the three vertices of the triangle.)

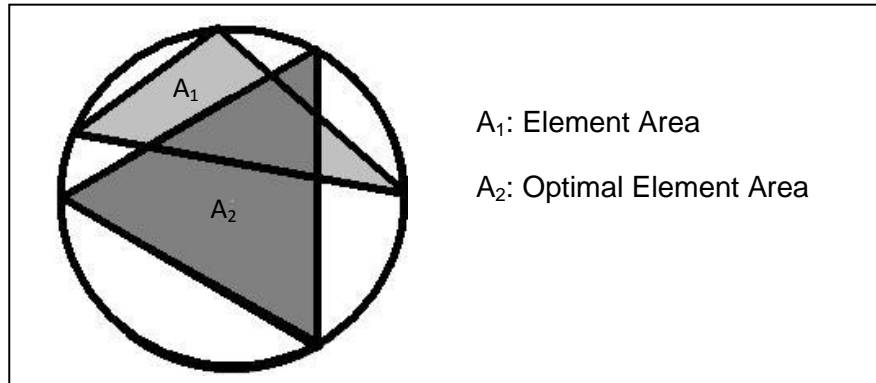


FIGURE II. 10: Shape factor

The Software also provides a table with the values that we can consider as acceptable in regard of the quality of the element. Thus, it can be considered valid all shape factors above 0.01, as (6) indicates.

Aspect ratio

The aspect ratio is the ratio between the longest and shortest edge of an element.

Abaqus/CAE highlights elements with an aspect ratio larger than a specified value. This value can be user defined, but as for shape factor, (6) gives a table with the recommendable values for the aspect ratio. In case of triangular elements, the recommendation is 10. Thus we will take 10 as our aspect ratio limit.

The aspect ratio gives us an idea of how regular our shape is. As it approaches 1 its geometry is more regular.

4.3. Results

Since no reference in the literature exists for the optimal mesh size, ten different values were computed and compared. The parameter to be analyzed is the maximum radius (in mm) of the circumference outside each triangle from the resulting mesh introduced before.

The values are integer numbers between 1 and 10, chosen in order to simplify the number of solutions to study.

The meshing process is carried out for all the values. Shape factor and aspect ratio are computed as well. The results can be seen in table II.1.

mesh size (mm)	1	2	3	4	5	6	7	8	9	10
SF average	0.7378	0.7023	0.7369	0.7343	0.7426	0.7421	0.7449	0.7516	0.7481	0.7550
SF worst	0.0409	0.0391	0.0538	0.0712	0.0690	0.0771	0.0459	0.0733	0.0771	0.0771
AR average	1.69	1.75	1.67	1.67	1.66	1.66	1.65	1.64	1.65	1.63
AR worst	4.60	4.77	4.32	4.33	4.38	4.02	3.97	3.70	3.71	3.92

TABLE II. 1: Meshing results

In table II.1, results from the meshing are shown. For every value of the maximum radius, the two geometrical parameters are calculated: Shape factor and aspect ratio. Since the values must represent all the triangles of the mesh, the average values are recorded. To ensure that the recommended limit is not transposing, the worst value of this parameters is also shown.

Recalling the limiting values given by the recommendations in (6), the shape factor should not be under 0.01; meanwhile the aspect ratio should be under 10. Following this recommendation, all mesh sizes should be accepted, but only one can be chosen.

The next figure is a representation of how the lung's visual aspect changes with different mesh sizes. Not all of them need be represented to show the evolution in the lung's details with respect to mesh size. In mesh size 1, we observe a very high level of detail; even the room for the ribs can be distinguished. However, the mesh is so small that is impossible to recognize if the element shape is triangular or not. When the mesh size is increased, the level of detail decreases, until at mesh size 10, the maximum size, not even the lung's root can be seen.

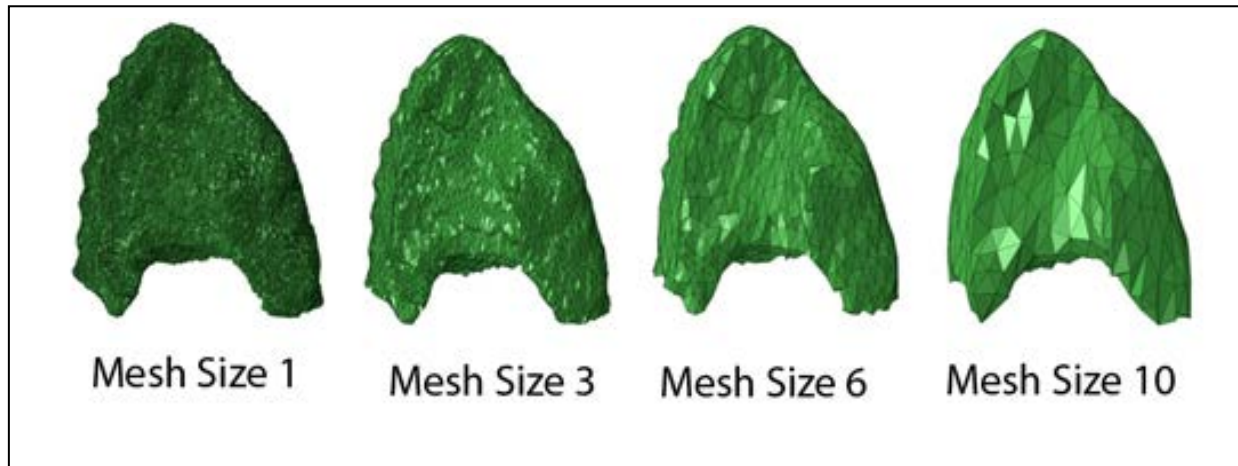
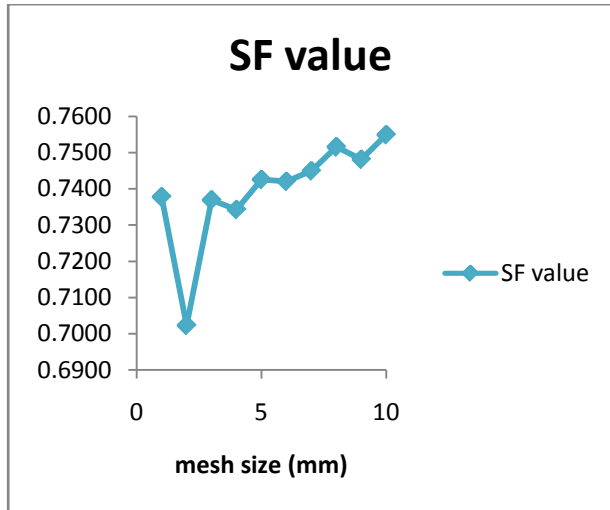


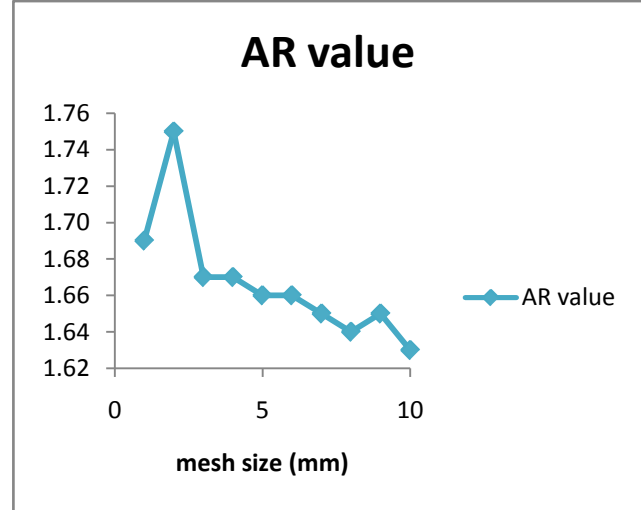
FIGURE II. 11: Mesh sizes

Mesh sizes 1, 3, 6 and 10 were chosen to represent the lung geometrical evolution.

The two main parameters that help us choose the final mesh size are the ones introduced before: the shape factor and the aspect ratio. The correlation between the two parameters and mesh size is best explained in a graph. As a first comparison, the average values were taken.



GRAPH II. 3: Sf. vs. Mesh size

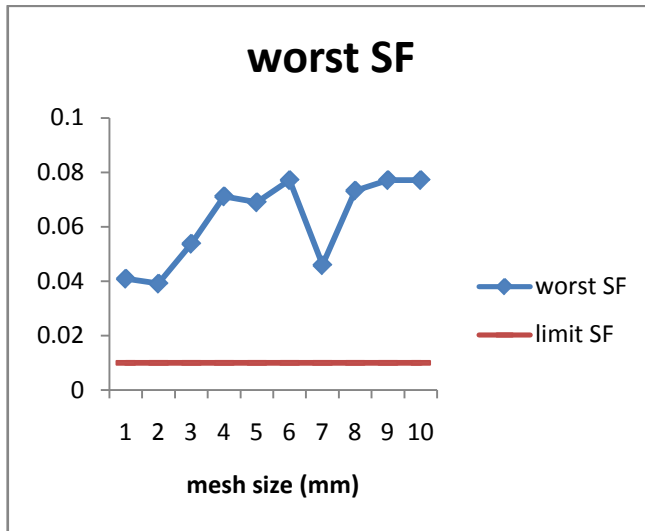


GRAPH II. 2: AR vs. Mesh size

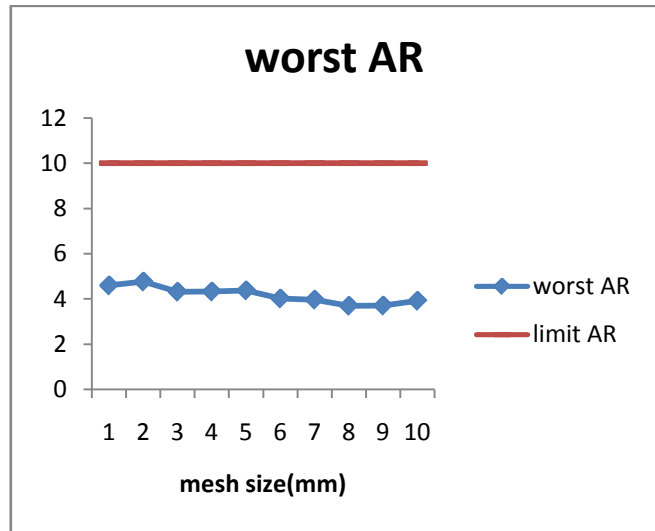
In graph II.2 the shape factor's progression can be seen. According to the shape factor definition, a shape factor of one is most ideal. All of the range of data is between 0.7 and 0.76, and the worst value allowed, according to recommendations of the finite elements software, is 0.01. No values are under the limit.

In graph II.3 the aspect ratio's progression can be seen. Similarly, the ideal aspect ratio is 1. All of the meshes have an AR between 1.76 and 1.62. The limit, in this case an upper limit, is recommended to be 10. No values are even close to the limit.

As no mesh sizes exceed the limits, all of them can be used in the simulation. In a more strict evaluation, the limits should be compared with the worst values to ensure that no triangles go over the limit. For that purpose, the graphs II.4 and II.5 were created.



GRAPH II. 4: Worst SF vs. Mesh Size



GRAPH II. 5: Worst AR vs. Mesh size

As was announced at first, even the value of the SF and the AR for the triangle with the worst geometry are inside the allowed limits. Now, we can ensure that, whatever mesh been chosen for the simulation, the software will be able to work with it regularly.

From graphs II.2 and II.3 the most notable mesh size is a size of 2 mm. Its average SF is lowest and its average AR is highest. In graphs II.4 and II.5 the lowest SF worst value correlates to the highest AR worst value. Thus we reject this mesh size as a possibility for our meshed lung.

The rest of the mesh sizes have very similar parameters values, so in order to avoid the unrealistic geometry given by coarse meshes, and the very long simulations with a very high number of elements given by fine meshes, we decide to vote for an intermediate SF value.

The average of the average SF values is 0.7437, hence we select the closest values, and these are the 5mm and 6mm mesh sizes (0.7426 and 0.7421 respectively). In order to pick one mesh size, we look at the AR values, which are the same in both cases (1.66). The final decision is determined by the worst values: mesh size = 5 mm has a corresponding worst SF value of 0.069 and 4.38 worst AR; mesh size = 6 mm has a corresponding worst SF value of

0.0771 and 4.02 worst AR. The worst values of the mesh = 5mm are inferior, thus the mesh size = 6 mm is elected to be the mesh size for the model.

Many other values could have been selected, for example 5.5mm; but for the moment, the mesh size will be 6mm.

5. SMOOTHING

5.1. Overview

Polygonal meshes (mostly triangle meshes) are created which represent the border surface of the desired structures in 3D space.

Due to slice-based discrete sampling and physical conditions of medical imaging, extracted surface models suffer from **artifacts** and thus only represent an approximation of the real patient anatomy. In medical applications, accuracy, volume preservation, and the conservation of distances between different surfaces is crucial as we introduced at the beginning of this project.

Artifacts are used to denote every missing or additional artificial object parts as well as frayed parts, holes, stairs and plateaus. The table II.2 shows a list of the most common artifacts in medical imaging.

Smoothing process has the main purpose of reduce or eliminate artifacts. It consists of mathematical algorithms applied to a three dimensional mesh.

Table II.2 contains even artifacts that cannot be reduced or eliminated by smoothing, (motion and signal artifacts). However, appropriate smoothing algorithms should cope with imperfect data and should not amplify these artifacts.

Exists several kind of smoothing algorithms, however, considering the specific requirements for medical visualization, it is not yet clear which mesh smoothing algorithms are appropriate for medical visualization in every organ and how it affects the results.

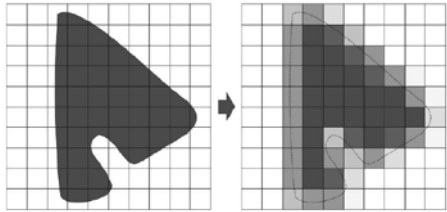
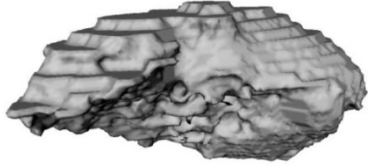
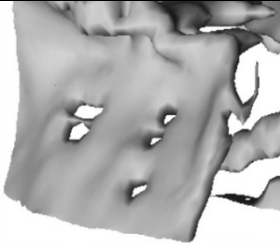


NOISE	
MOTION AND SIGNAL ARTIFACTS Due to the movement of the patient, or the implants that block out the X-ray beam (in CT) or that provoke in-homogeneities in the magnetic field (MRI)	
PARTIAL VOLUME EFFECT Due to discrete resolution of the image acquisition	
BLOCK/STAIRCASE Due to the binary classification as a result of the <i>segmentation</i> * process	
HOLES Due to under-segmentation	
FRAYED PARTS Due to over/under-segmentation	
ADDITIONAL/DETACHED PARTS Over/under-segmentation	

TABLE II. 2: Fundamental artifacts in medical imaging

* **Segmentation** is when each voxel of the volume data is classified as part of a specified object or a part of the background. (Binary classification: 1 = part of the object, 0 = background). Due to artifacts of the image acquisition process, segmentation can fail and result in what is known as **over-segmentation**, too many voxels are classified as being part of an object; and **under-segmentation**, too few voxels are classified as being part of an object.

In this point on the project, the most appropriated lung mesh smoothing is researched, comparing the *laplacian*, *laplacian + HC* and *Low Pass* mesh smoothing algorithms.

LAPLACIAN MESH SMOOTHING ALGORITHM:

The laplacian filter is the simplest mesh-smoothing algorithm. Iteratively, traverses all the surface vertices and moves each vertex into the geometric center of its topological neighbors. Figure II.6 shows an example of topological neighbors, also known as umbrella region.

This process is called pure laplacian smoothing, and the equation (Eq.II.50) shows the main step in the algorithm. The new smoothed position p' , results from its old position p and its neighbors, q_i . The total number of neighbors is given by n .

$$p' = p + \frac{1}{n} \sum_{i=1}^n q_i \quad (\text{Eq.II.50})$$

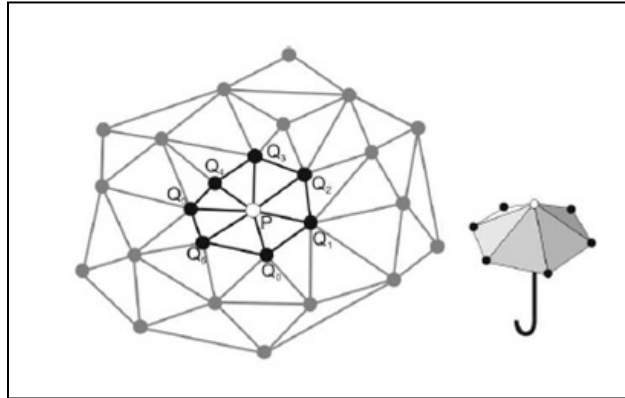


FIGURE II. 12: Direct Neighborhood

Topological neighborhood (umbrella region) of a polygonal mesh.

This procedure can be repeated iteratively until the desired smoothness is achieved. Often a weighting factor λ is introduced as an improvement added to the algorithm. This factor regulates the effect of the direct neighbors on the new position of the current vertex. Equation (Eq.II.51) governs this procedure.

$$p' = (1 - \lambda) \cdot p + \frac{\lambda}{n} \sum_{i=1}^n q_i \quad (\text{Eq.II.51})$$

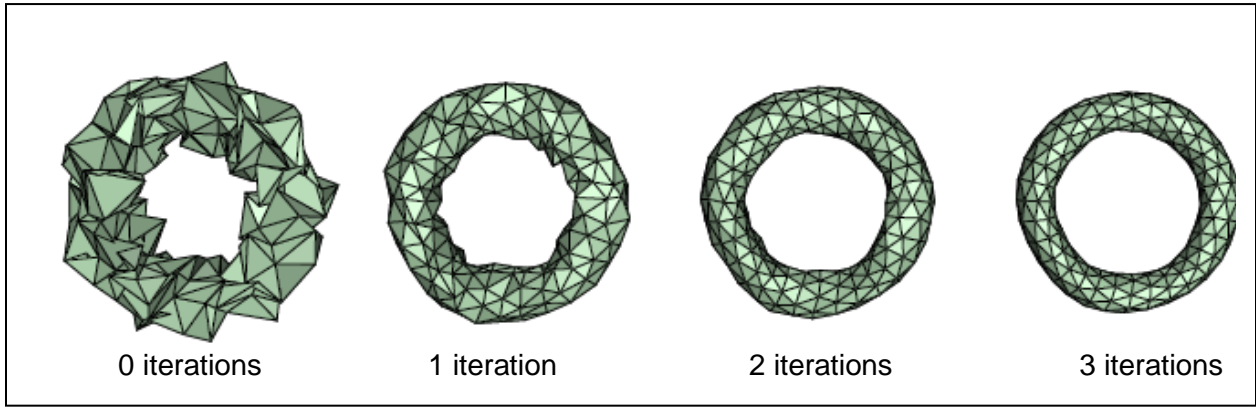


FIGURE II. 13: Laplacian algorithm

Laplacian algorithm applied to a noisy torus after 1, 2 and 3 iterations. We can recognize a strong degree of shrinkage.

This procedure can be repeated iteratively, until the desired smoothing is reached. As is shown in figure II.12, a volume diminution takes place with every iteration during laplacian smoothing process. If the number of iterations goes to infinity, the mesh will be shrinking down to a point.

LAPLACIAN + HC MESH SMOOTHING ALGORITHM:

The idea of the HC-algorithm (*HC* stands for *Humphrey's Classes*) is to push the modified points (produced by the laplacian algorithm) back towards to their former position.

The algorithm starts applying the pure laplacian smoothing given by equation (Eq.II.50). After that, an improvement of laplacian smoothing, and backward movement are both simultaneously carried out, according to equation (Eq.II.52).

$$b = p' - (\lambda \cdot o + (1 - \lambda) p) \quad (\text{Eq.II.52})$$

In this equation p' denotes the position after the pure laplacian operation, o the original position (before any smoothing process), and p the position given by the previous iteration.

The final position of p is given by the weighting of the backward movement of the corresponding point, and its neighbors' backward movement. The weighting is regulated by a factor, $\beta \in [0,1]$ similar to laplacian weighting factor λ . Equation (Eq.II.53) gives the final position.

$$p_{final} = p' - \left[\beta \cdot b + \frac{1 - \beta}{n} \sum_{i=1}^n b_i \right] \quad (\text{Eq.II.53})$$

To avoid a four dimensional search for this filter, we set $\beta = 0.2$, so that the own displacement backward vector contributes with a factor of 0.2 and the mean displacement

backward vector of the neighborhood with a factor of 0.8 to the final position, as indicates the literature (7).

LOWPASS MESH SMOOTHING ALGORITHM:

The low pass filter represents a combination of two laplacian-like filters, one with a positive weighting factor and the other one with a negative factor that are executed alternating. The new position p' of all vertices results here from its old position p and its neighbors q as shown in equation (Eq.II.54):

$$p' = (1 - \lambda)p + \frac{\lambda}{n} \sum_{i=1}^n q_i \quad (\text{Eq.II.54})$$

In contrast to the laplacian filter, with the low pass filter, is carried out in two steps: a standard laplacian smoothing with a weighting factor λ is applied first. In the second step, the laplacian filter is applied again but now λ is replaced by μ , while μ is set to a value a little bit smaller than $-\lambda$. In our case, μ is set to $\mu = -1.02\lambda$ as inspired by (7).

5.2. Implementation

Before comparing the different smoothing algorithms, it is necessary to establish a set of consistent criteria that help to evaluate the results. To do this, we make use of the mesh smoothing requirements for medical visualizations, introduced by R.Bade et al. in (7). These criteria are based mainly in two requirements: Visual improvement, because the primary goal of mesh smoothing is to achieve a visual improvement of the target's surface, and minimum error according to the original model.

To assess if a mesh smoothing strategy meets both requirements listed above, some criteria that guarantee the suitability are listed:

- **Visual improvement** when a visual inspection is carried out. This is a task which seeks the elimination of potential artifacts as well as non-distortion of the mesh elements, in other words, quality of the triangular elements composing the surface mesh. This is measured in ABAQUS, with what was introduced before as *shape factor*. Since smoothing process is a method that improves mesh quality, we are going to fix a minimum rate of shape factor required in the final mesh: Our reference value it is 0.75.
- **Difference between the volume** of the smoothing surface and the original. So we can ensure the small degree of shrinkage. We set a -6.5% as limit of volume shrinkage, basing on literature.

- A third criterion is to take into account the **computational time** required for the smoothing process. It can be useful to choose an algorithm in situations when all criteria established in (7) are fulfilled by different strategies.

The lung meshed shown in the next figure shows some different artifacts like frayed parts, plateaus or staircase. It is smoothed under the three different algorithms mentioned before. The results are shown in the next section.

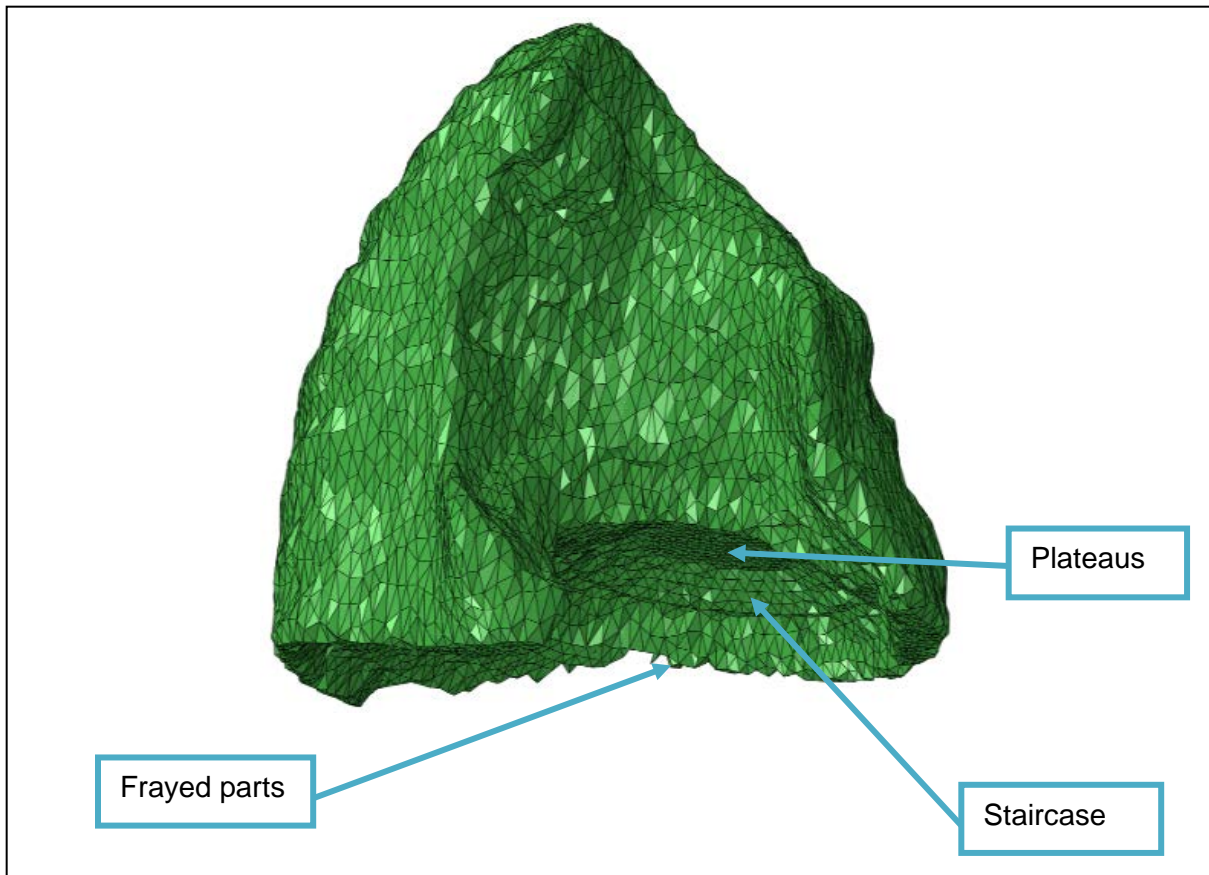


FIGURE II. 14: Meshed lung

Some artifacts are easily recognized, as staircase, frayed parts or plateaus.

For the implementation of the algorithms, the function *smoothsurf* is used, from the toolbox *iso2mesh*, in MATLAB. To call this function, several input parameters are needed. The main ones are:

- Node coordinates of the surface mesh to be smoothed.
- Smoothing method. It can be 'laplacian', 'laplacianhc' or 'lowpass'.
- Number of iterations and weighting factor in the smoothing process.

5.3. Results

In this section the smoothing results of the different filters are presented and discussed. Following the literature (7) and (8), each smoothing method is evaluated with four different iteration steps (5; 10; 20; 50) and six weighting factors (0.05; 0.1; 0.3; 0.5; 0.7; 0.9).

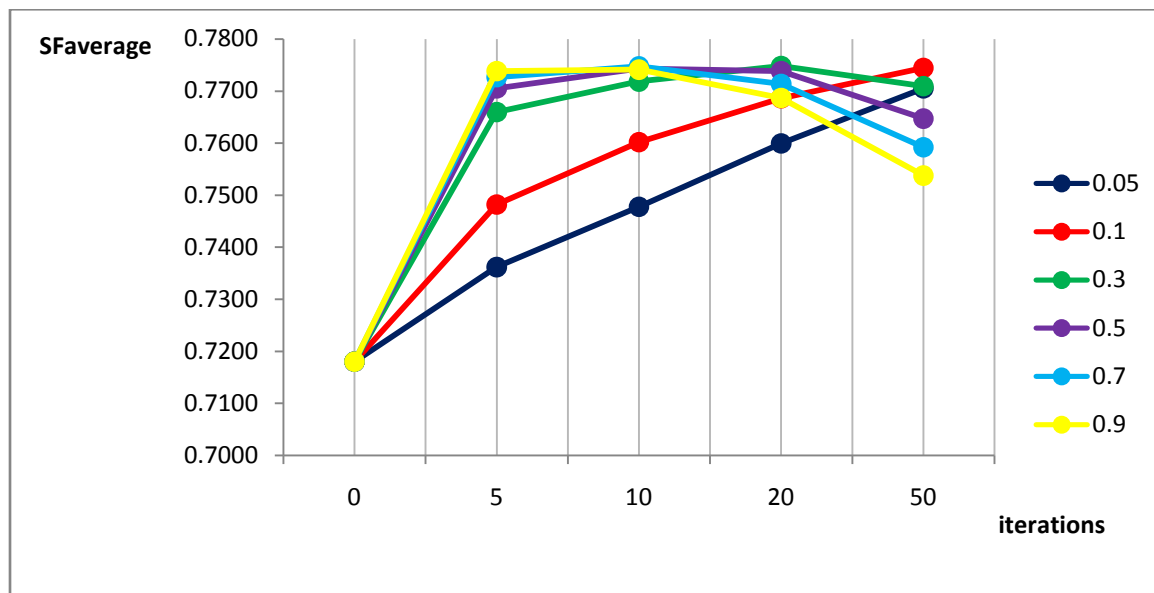
The two first criteria of improvement measurement (average shape factor and degree of shrinkage), are shown in graphs, meanwhile the computational time required for each result is presented in a table.

RESULTS FOR THE LAPLACIAN SMOOTHING:

The laplacian smoothing implemented was the algorithm given by equation (Eq.II.51). This is a process that takes into account both the previous position and the neighbors' positions.

Visual improvement measure: SHAPE FACTOR.

In graph II.6 we can see the evolution of the shape factor versus the number of iterations carried out in the laplacian smoothing algorithm.

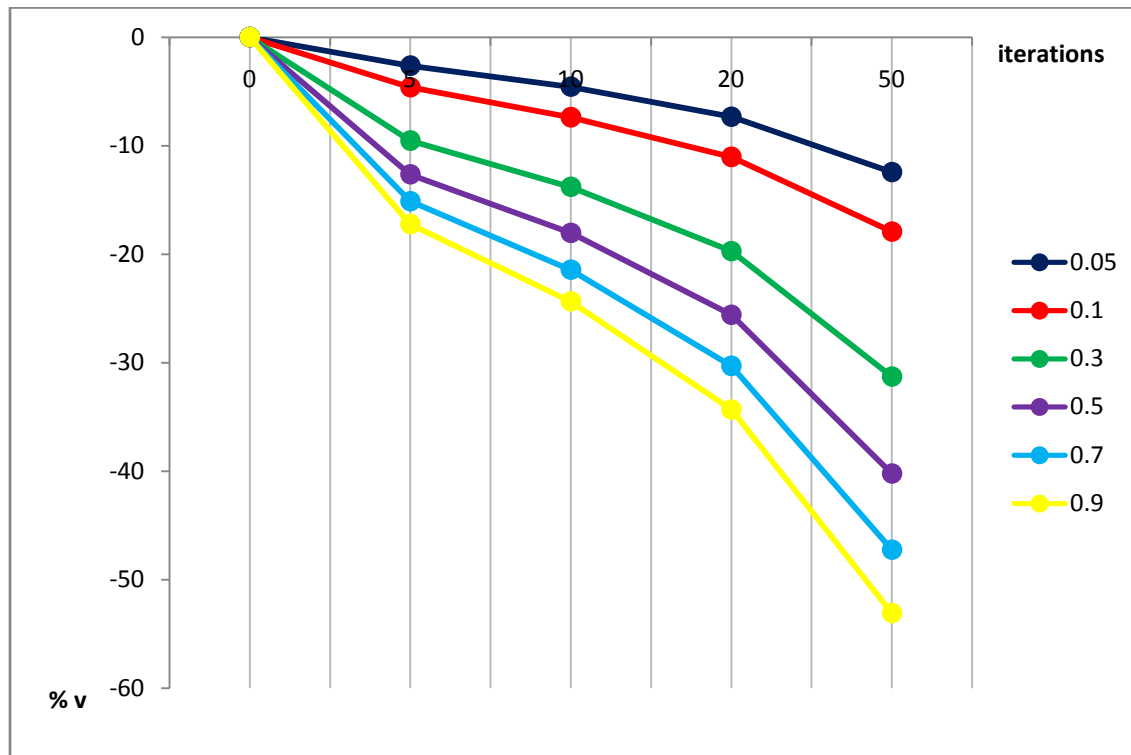


GRAPH II. 6: SF vs. Iterations in Laplacian smoothing

For each weighting factor we get a different curve. For smaller weighting factors (0.05, 0.1), the shape factor always increases with the number of iterations. For medium and larger parameters (0.3, 0.5, 0.7 and 0.9) the mesh quality starts to decrease after 10 iterations. This fact can be explained looking at next measurement parameter: degree of shrinkage.

Difference between volumes: DEGREE OF SHRINKAGE:

As we saw in the initial introduction to the laplacian smoothing algorithm, a high degree of shrinkage takes place as we increase the number of iterations in the process. (See figure II.12). In graph II.7 the percent of decreased volume is plotted.



GRAPH II. 7: Degree of shrinkage vs. iterations in laplacian smoothing

More than 50% of shrinkage is registered in some of the results for this smoothing method. This explains the shape factor drop from 10 iterations: For weighting factors 0.3, 0.5, 0.7 and 0.9 the rate of volume decrease is so high that the triangular mesh starts to deform. This can be deduced from equation (Eq.II.51): The larger the weighting factor, the less influence the position in the last iteration has, and the more influence the surrounding nodes have.

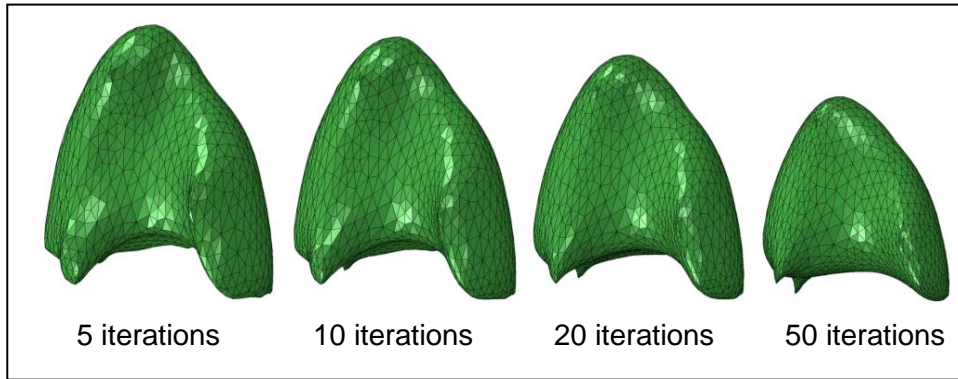
COMPUTATIONAL TIME:

With respect to the computational time, this algorithm is very fast. No more than 4 seconds are required for 50 iterations. Table II.3 details all time measurements.

iterations	0	5	10	20	50
$\lambda = 0.05$	0	0.5468	0.9120	1.6317	3.7610
$\lambda = 0.1$	0	0.5526	0.9090	1.6055	3.7365
$\lambda = 0.3$	0	0.5549	0.9128	1.6265	3.7542
$\lambda = 0.5$	0	0.5569	0.9068	1.6213	3.7395
$\lambda = 0.7$	0	0.5579	0.9140	1.6254	3.7869
$\lambda = 0.9$	0	0.5486	0.9160	1.6101	3.7414

TABLE II. 3: Computational time in seconds for laplacian smoothing

Despite the good results obtained quickly for this algorithm, we must discard it, due to the high degree of shrinkage observed. It is necessary to realize a final shape that is very close to the geometry of a real organ. Figure II.14 shows the evolution of the lung geometry as the number of iterations is increased. The weighting factor, λ , is 0.7 for this example.

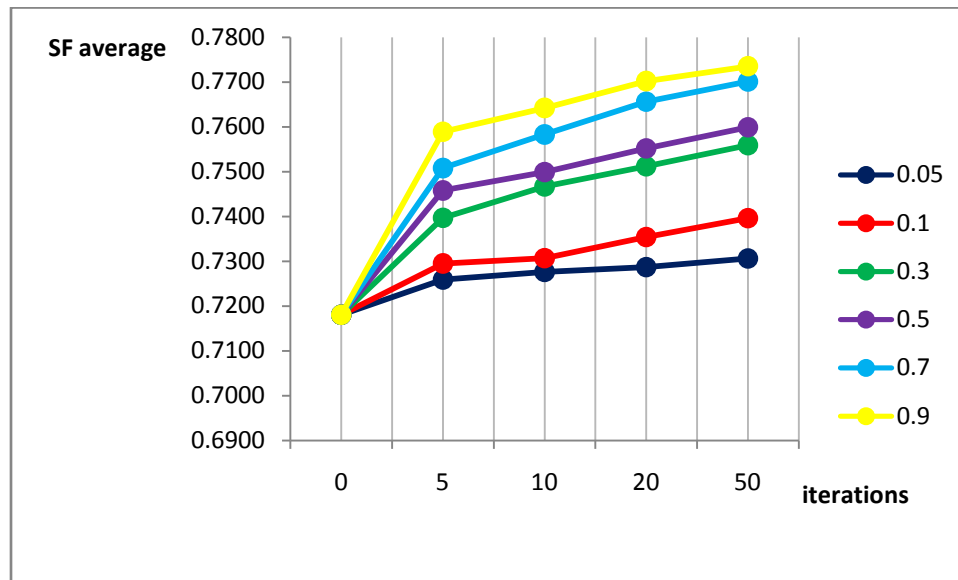
FIGURE II. 15: Laplacian algorithm smoothing results. $\lambda = 0.7$.

RESULTS FOR THE LAPLACIAN HC SMOOTHING

As mentioned in the last section, we set the backward movement weighting factor to $\beta = 0.2$. The algorithm we computed is represented by the equations (Eq.II.50), (Eq.II.52), and (Eq.II.53).

Visual improvement measure: SHAPE FACTOR.

In graph II.8 we can see the evolution in the shape factor. In contrast to laplacian smoothing, the laplacian hc smoothing algorithm never results in the shape factor decreasing; it always grows, reaching a maximum of 0.7735 for the weighting factor 0.9 at 50 iterations.



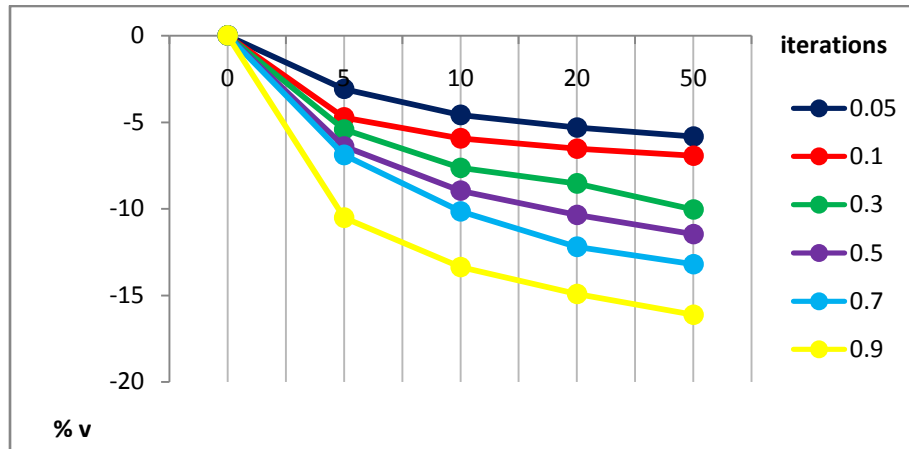
GRAPH II. 8: SF vs. Iterations in laplacian hc smoothing

Such a high mesh quality predisposes us to select the laplacian hc algorithm as a feasible smoothing algorithm for the lung mesh. Furthermore, since no decrease of SF occurs, we can conclude that no deformation in the mesh is taking place.

Difference between volumes: DEGREE OF SHRINKAGE:

For our purpose, the shrinkage rate is more important than the shape factor. Our goal is to produce a final shape that is as close as possible to the original shape. In graph II.9 the progression of the decreasing volume is shown for every weighting factor.

The graph shows the progression of decreased volume after the smoothing process. Based on our criterion of a maximum of -6.5% rate in the volume decreased, an acceptable shrinkage is obtained for weighting factors of 0.05 and 0.1.



GRAPH II. 9: degree of shrinkage vs. Iterations in laplacian hc algorithm

After looking at graph II.9, this method can be rejected. The degree of shrinkage is over the limit in 0.3, 0.5, 0.7 and 0.9 weighting factors after 5 iterations. Apply a smoothing process with only 5 iterations does not give to an improvement in mesh quality visually as we see in figure II.15.

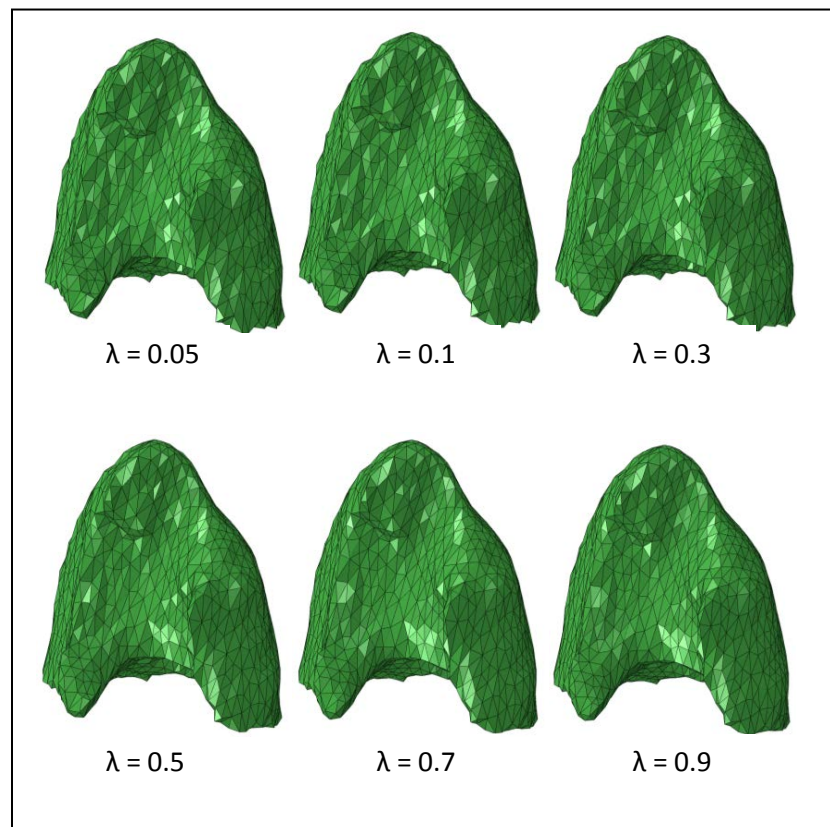


FIGURE II. 16: Five iteration smoothing for laplacian hc algorithm

Applying 5 iterations of laplacian hc algorithm we don't get any visual improvement for any of all parameters

COMPUTATIONAL TIME:

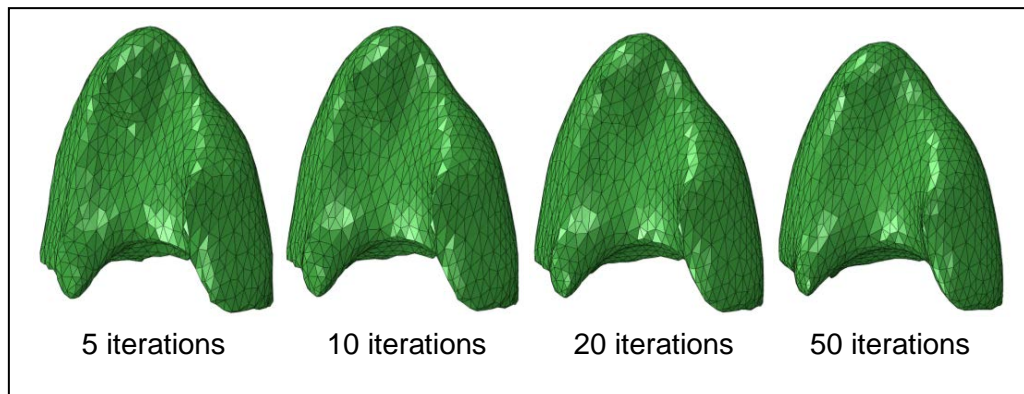
Computational time is a little bit longer with this algorithm than with the laplacian algorithm. That was expected, since the laplacian hc algorithm is obtained by starting with a laplacian algorithm and adding an additional routine for the backward movement.

iterations	0	5	10	20	50
$\lambda = 0.05$	0	0.9201	1.149	2.1028	5.0382
$\lambda = 0.1$	0	0.6561	1.1485	2.133	5.0544
$\lambda = 0.3$	0	0.647	1.1356	2.1528	5.0949
$\lambda = 0.5$	0	0.6566	1.1416	2.1092	5.0236
$\lambda = 0.7$	0	0.6538	1.1419	2.1291	5.0549
$\lambda = 0.9$	0	0.6563	1.143	2.1093	5.0503

TABLE II. 4: Computational time in seconds for laplacian hc smoothing

As a result, we can say that this smoothing method provides us with high SF values for higher weighting factors, 0.5, 0.7 and 0.9 0.7599, 0.7701, 0.7735 for 50 iterations respectively. On the other hand, those good values are host in not allowed shrink rates. This fact alone is enough to make us reject the method.

In figure II.16 we can see the progression of the mesh as we increase the number of iterations. In order to compare this algorithm with the laplacian algorithm we choose again $\lambda = 0.7$. A lesser degree of shrinkage is obtained with this method.

FIGURE II. 17: Laplacian hc algorithm smoothing result. $\lambda = 0.7$.

RESULTS FOR THE LOW PASS SMOOTHING

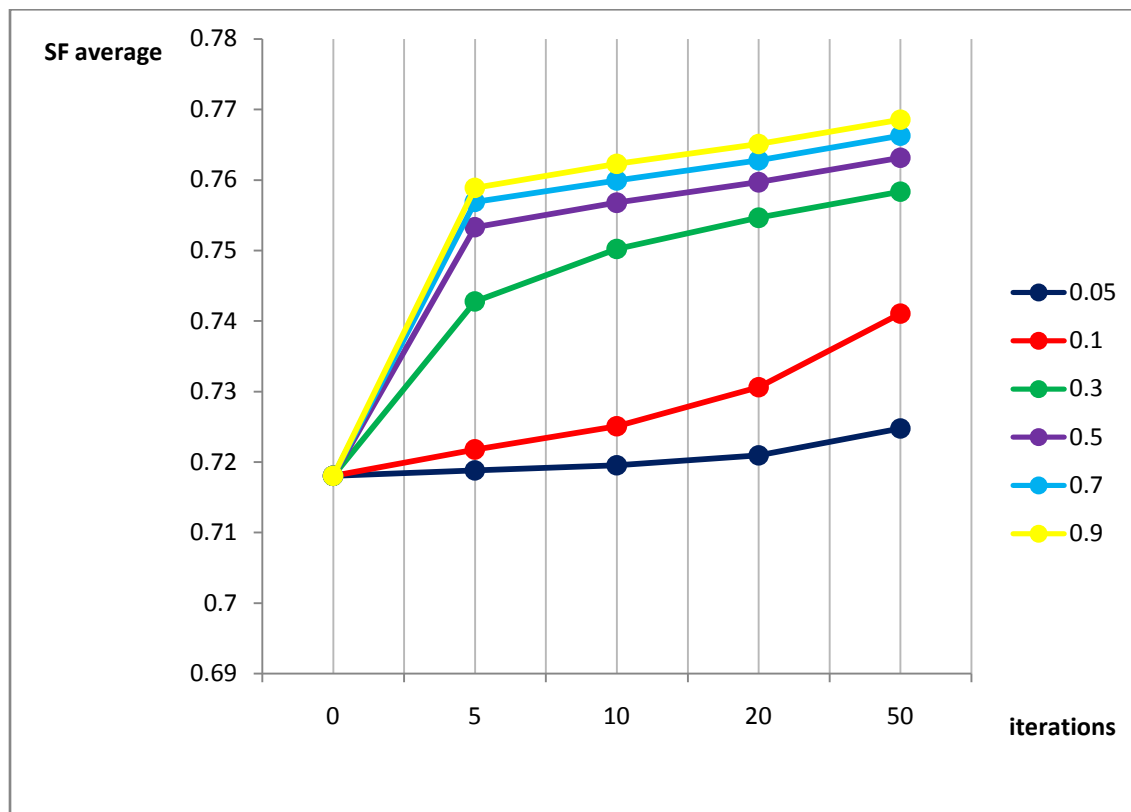
The last method we studied is the low pass smoothing method. Equation (Eq.II.54) governs the main algorithm and a backward movement is included in it, as in laplacian hc smoothing. The main differences between the two algorithms are the weighting factor in the backward movement and the method of ponderation for such a backward movement.

The implementation of the low pass filter is simpler, as the equations show: (Eq.II.50), (Eq.II.52) and (Eq.II.53) in laplacian hc, versus (Eq.II.54) in low pass.

Additionally, low pass filter gives a weighting factor in the backward movement proportional to the main weighting factor. Because of that, the ponderation of the back displacement vector is more easily computed than in the laplacian hc.

The next graphs show the results of applying the aforementioned algorithm to the meshed lung.

Visual improvement measure: SHAPE FACTOR.



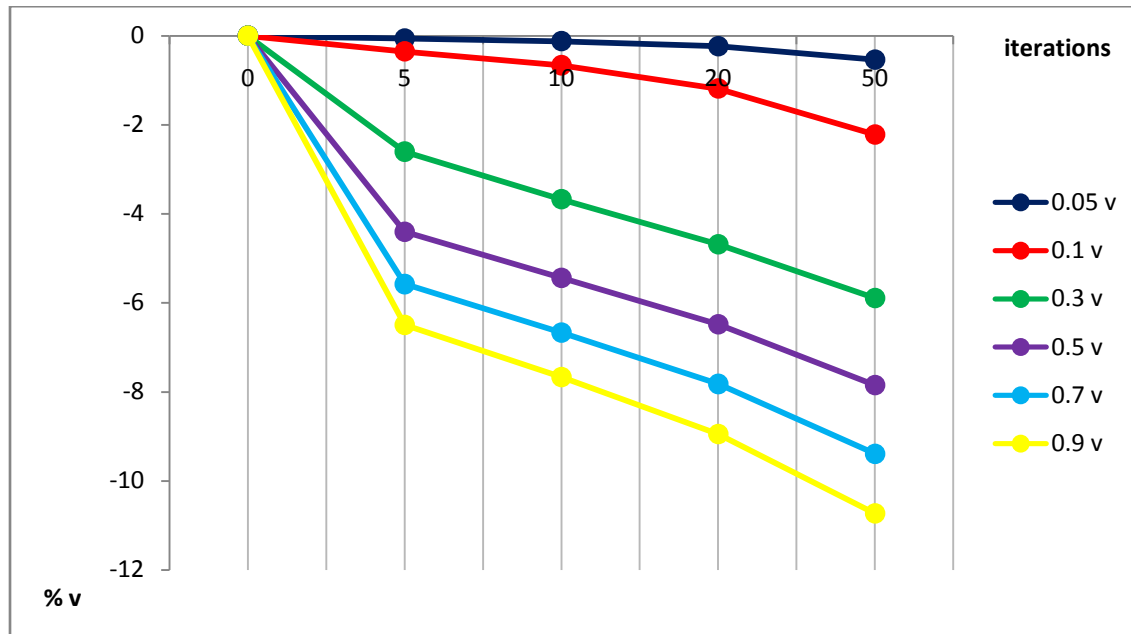
GRAPH II. 10: SF vs. Iterations in low pass smoothing

As occurred in the laplacian hc algorithm, the SF increased with the number of iterations and higher weighting factors. Acceptable SF values are achieved in this method for weighting factors 0.5, 0.7 and 0.9. A maximum is hit at 0.7685, with $\lambda = 0.9$ and 50 iterations.

According with the mesh quality measurement, both laplacian hc and low pass methods follow the same trend: the higher the number of iterations and the higher the weighting factor, the better the resulting SF value will be.

Difference between volumes: DEGREE OF SHRINKAGE:

The laplacian hc algorithm was found to be an unacceptable smoothing method due to its high shrinkage whereas the low pass algorithm does not reach shrinkage over -10.8%.



GRAPH II. 11: Degree of shrinkage vs. Iterations in low pass smoothing

Several values are under the limiting degree of shrinkage. They may prove valuable in the search for final smoothing methods. This method is, so far, the most appropriate smoothing algorithm. But before choosing a final method, we need to compare the last of the comparison parameters: Computational time.

COMPUTATIONAL TIME:

No significant differences were observed between the computational time in the laplacian hc algorithm and the low pass smoothing algorithm. Computational time does not seem to have an important role in smoothing algorithm selection. Since all of the results are quite similar and consistent with theory, we based our selection on the other two parameters.

Despite time being irrelevant in selecting an algorithm, we show in table II.5 the computational time needed, as we did for the other two methods.

iterations	0	5	10	20	50
$\lambda = 0.05$	0	0.703	1.1886	2.1647	5.1083
$\lambda = 0.1$	0	0.6936	1.2005	2.196	5.1493
$\lambda = 0.3$	0	0.6863	1.1882	2.176	5.1508
$\lambda = 0.5$	0	0.6965	1.1836	2.2004	5.1683
$\lambda = 0.7$	0	0.6959	1.1907	2.2315	5.1405
$\lambda = 0.9$	0	0.693	1.1941	2.1736	5.1047

TABLE II. 5: Computational time in seconds for low pass smoothing

Laplacian and laplacian hc have been previously rejected for several reasons. The low pass filter has shown satisfactory results, thus it will be the smoothing process applied. Once the smoothing process is decided, the next step is fixing the weighting factor and the number of iterations carried out. For that, we will get information of graphs II.10 and II.11.

From graph II.10 we can discard lower weighting factors (0.05 and 0.1), because of its low mesh quality: under 0.75.

Graph II.11 provides information about the degree of shrinkage. As we announced before, this is likely our most important parameter. A specific analysis will be done in order to eliminate undesirable results. A high degree of shrinkage exists for $\lambda = 0.9$ starting at -6.49% at 5 iterations and increasing with the number of iterations, so this parameter is eliminated from our list of possibilities.

We study parameters 0.3, 0.5 and 0.7 in more depth. In table II.6 we can compare the values of the shape factor, and the volume reduction for these weighting factors.

lamdba	iterations	5	10	20	50
0.3	SF average	0.742789	0.75023	0.754661	0.758347
	V (%)	-2.6033	-3.6729	-4.6853	-5.8914
0.5	SF average	0.753301	0.756769	0.759661	0.763127
	V (%)	-4.4045	-5.439	-6.4821	-7.8469
0.7	SF average	0.756895	0.759931	0.762793	0.766285
	V(%)	-5.5767	-6.6656	-7.8198	-9.3881

TABLE II. 6: Smoothing methods

The methods that pass the shrinkage and SF limit and SF are marked in yellow. Seven possibilities are found to be suitable. In lieu of more criteria, we based our final decision on the higher shape factor for a smoothing process. That is: a weighting factor of 0.5 and 20 iterations.

Figure II.17 shows the progression of the final smoothing process. The mesh is smoothed with a weighting factor of 0.5, and the number of iterations is gradually increased.

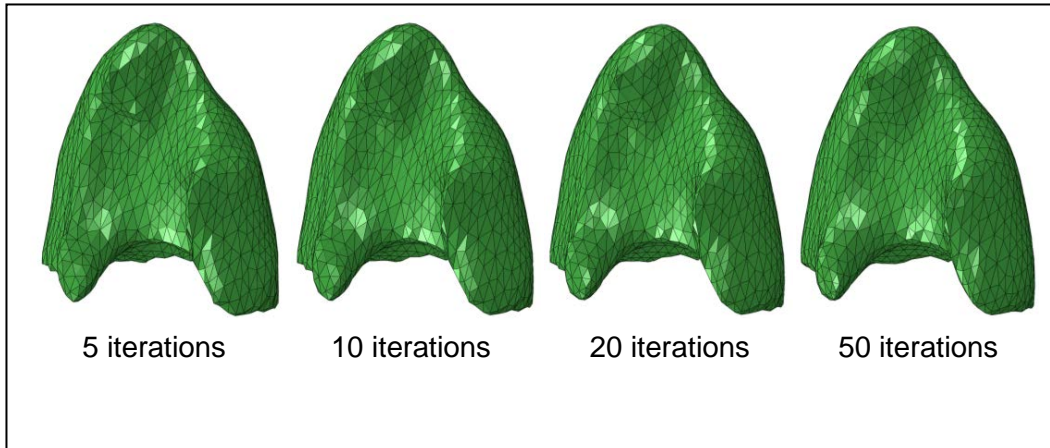


FIGURE II. 18: Low pass algorithm smoothing results. $\lambda = 0.5$

6. LUNG FINAL MODEL

Thus far, we have defined meshing and smoothing. Both operations have been utilized in a three-dimensional surface mesh formed by triangular elements.

The next step carried out was the conversion of the triangular mesh surface in a volume of tetrahedral elements to obtain a homogeneous solid. This process was done automatically in Abaqus. For the model lung selected, the process obtained a total amount of 2847 nodes forming 12906 tetrahedral elements.

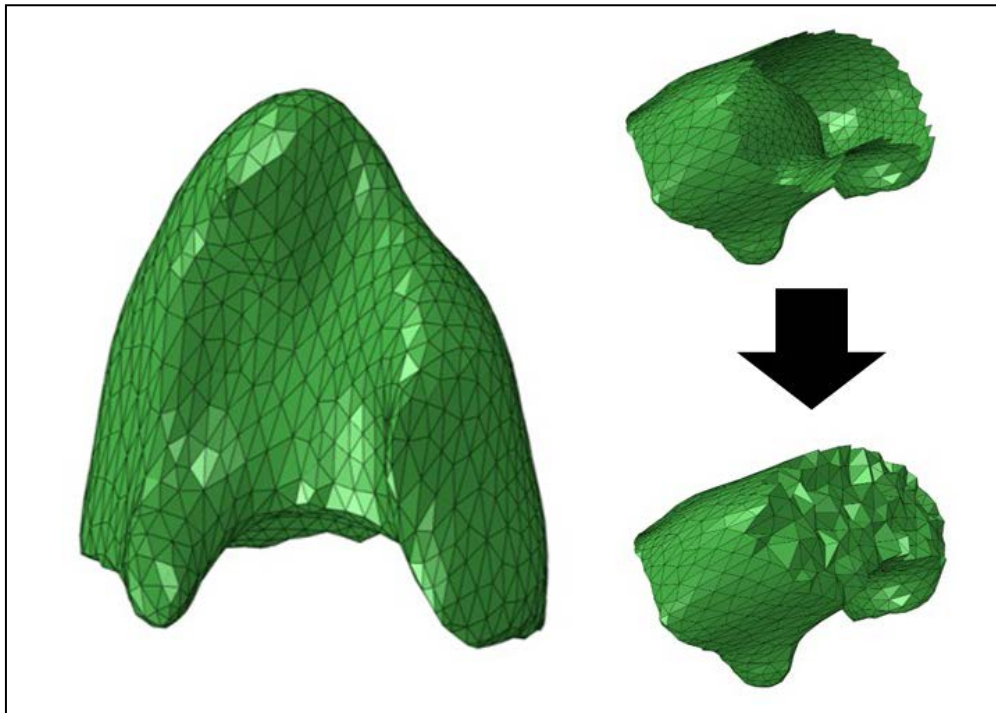


FIGURE II. 19: Lung internal meshing

From a surface triangular mesh, we get a tetrahedral volume mesh

The values of the tetrahedral mesh quality were also tested. For tetrahedral elements, Abaqus sets in (6) the following limit of quality: shape factor less than 0.0001 and aspect ratio less than 10.

In our mesh, the next values were obtained for the average and the worst quality of the parameters:

	Shape factor	Aspect Ratio
Average value	0.626830	1.71
Worst value	0.012892	5.07

TABLE II. 7: Mesh quality values.

Mesh quality values, in our final tetrahedral Meshed volume

Ostensibly, we could have carried out a volumetric mesh from the beginning and apply the smoothing operation to that volume, but we decided instead to mesh the volume after the smoothing process and optimize it later.

With an early mesh, the number of elements that would have resulted would be very high, thus, despite the fact that smoothing is a surface operation, it would affect to the internal elements too. That is because smoothing moves the nodes positions backwards, so that tetrahedral elements with a face on the surface would have been somewhat deformed. That in turn could have resulted in worse values in mesh quality parameters compared to the chosen, aforementioned procedure.

To complete the lung model, it remains to assign mechanical properties to the model: elasticity modulus, E , and Poisson's ratio, ν . In the absence of a procedure that we could carry out in practice to obtain these values, it was decided to refer to the literature. As example, the following table shows the parameters used in the different references.

Ref.	E	ν
(9)	4kPa	0.35
(10)	1kPa	0.38
(11)	5kPa	0.45
(12)	0.25MPa-1 kPa	0.1-0.4
(13)	0.1MPa	0.35
(14)	6kPa	0.4

TABLE II. 8: Mechanical properties in the literature

Values assigned in the literature for different biomechanical models of the lung

According to the values of the parameter proposed in the previous table, the values range from 0.25 MPa to 1.0 kPa for the elasticity modulus and 0.1 to 0.45 for Poisson's ratio. There is no consensus on the values between authors. In this pilot study, for simplicity reasons, the lung was modeled as linear isotropic elastic material and Young's modulus and Poisson's ratio were chosen to be 0.12 MPa and 0.3 respectively.

There is not much relevance in the parameters' values due to the behavior in a linear isotropic elastic material: Increasing elasticity modulus E and/or Poisson's ratio ν produces stiffer response to external forces; thus higher E and ν values should require higher pressure applied to reach the displacements we aimed for.

At this point, it is important to remember that our main and final goal is obtaining the displacement field leading to the lungs in the EE state to the EI state.

PART III: SIMULATION

This part will explain the entire process carried out for the simulation. We will begin to explain the developed numerical model, and we will show results of the simulation.

The program used for the simulation was Abaqus, but a similar program may have been suitable.

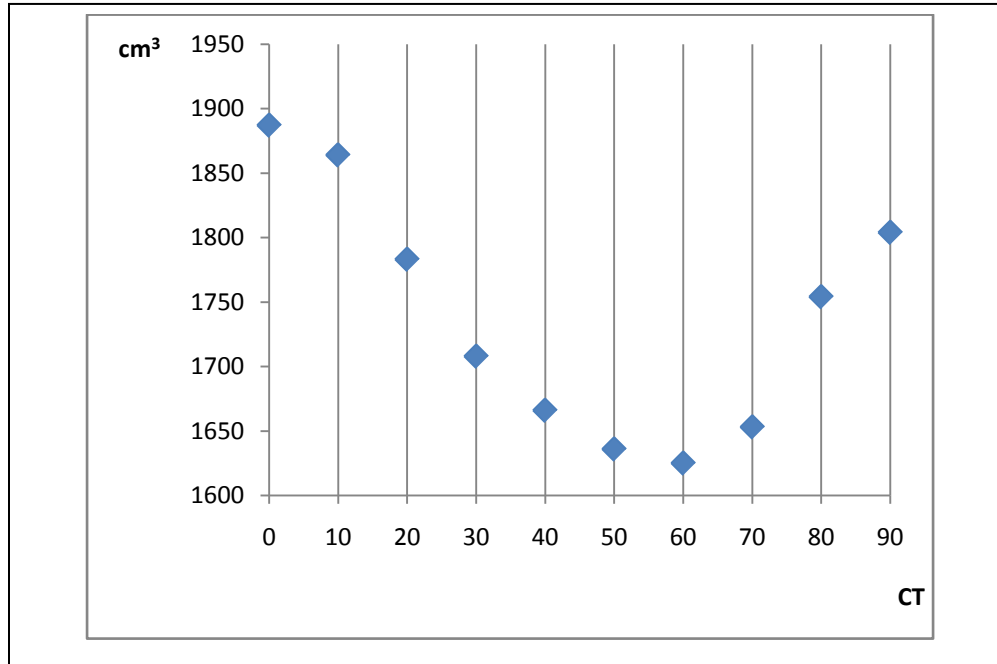
1. NUMERICAL MODEL

Once geometry of the lung is well-defined, we proceed to explain the numerical model.

As explained in the corresponding section, the model approach is based on two geometries of the lung: one internal, representing the initial state, EE, and one external, representing the final state, EI. Once the parameters of meshing and smoothing and the elastic properties of the geometry are defined, we proceed to identify the two phases of the breathing process which correspond to the previous states.

To do this, we proceed to measure the volume enclosed by the 3D surface in each of the phases of the breathing, eventually obtaining what is shown in graph III.1.

Each of the phases is named according to the following pattern: CTX0, where the number X designates the current phase, starting in phase 0, and ending in phase 9. The abscissa axis represents the phases, and the y-axis, the volume obtained in cm^3 .



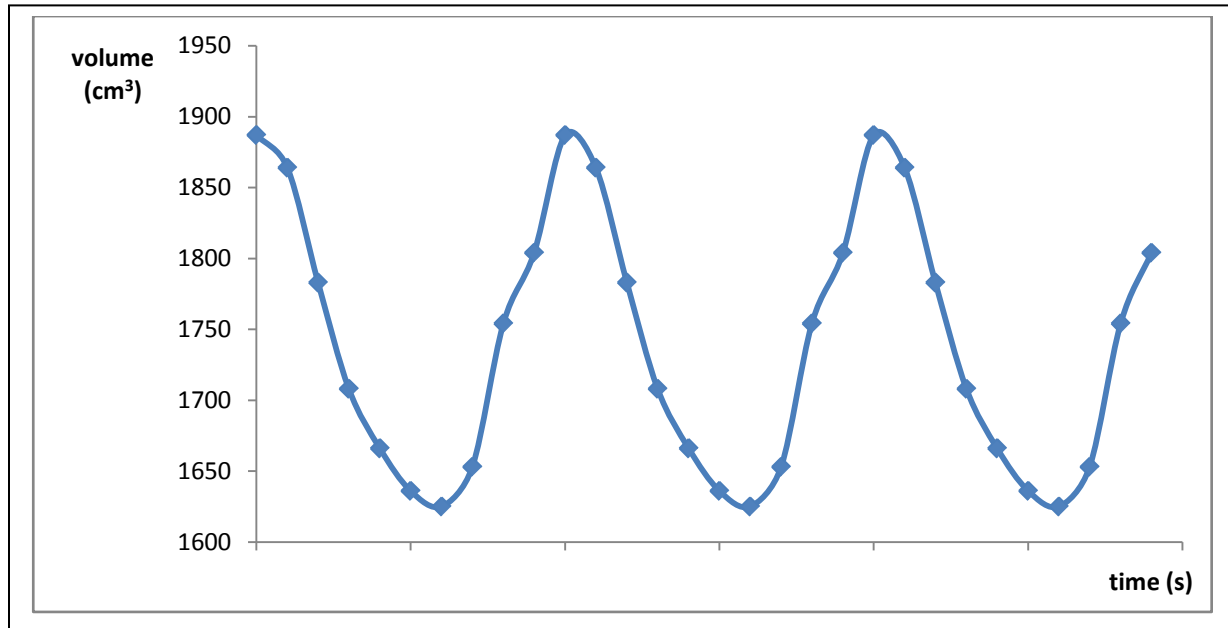
GRAPH III. 1: Lung volume in every breathing phase

The volume is obtained for each phase with the function *elemvolume*, of the *iso2mesh* tool, which is based on the general formula for calculating the volume of a tetrahedron. From the cartesian coordinates (x, y, z) of three of its vertices A, B and C, we can get the volume of a tetrahedron, regardless of whether or not it is regular. This is equal to one sixth of the scalar product of the first vector and the vector product of the other two as we can see in equation (Eq.III.1).

$$V = \frac{1}{6} \begin{vmatrix} x_A & x_B & x_C \\ y_A & y_B & y_C \\ z_A & z_B & z_C \end{vmatrix} \quad (\text{Eq.III.1})$$

From graph III.1 we can easily deduce which phases are corresponding to our initial and final states. The state EE (End of expiration) corresponds to the CT60 phase, since at this phase the minimum volume of the lung is reached. Similarly, the maximum volume is assigned to the state EI (End of expiration), and this phase corresponds to CT00.

We represent the curve of the breath. Although graph III.1 cannot be seen very well, if we repeat the pattern that follows the volume enclosed by the geometry, we see a nearly sinusoidal waveform in the volume evolution. This can be seen in graph III.2.



GRAPH III. 2: Breathing curve

Having defined the initial and final states, we allocate properties. The geometry for the EE state will assign a 3D tetrahedral mesh with Young's modulus 0.12 MPa and Poisson's ratio 0.3, as we defined in the part II: model lung.

In contrast, the geometry corresponding to the EI state acts as a limiting geometry. It is a 3-dimensional surface formed by triangular elements like a shell, to which we assign more stiffness properties than in the case of the EE state to ensure that there is no penetration during lung expansion of the limiting geometry.

As for other phases, they will not be necessary for the remainder of the model's development. From this point on, we will only work with the geometry corresponding to the EE state and with the tridimensional surface of the EI state with the characteristics described above.

The next step is to "join" the two states and work with them as a single set. The EE volume and EI surface have different maximum heights as observed in figure III.1. In the EE state with less volume, we can see at the left size of the figure III.1 is over the EI state. The EI state encloses more volume and it is shifted down.

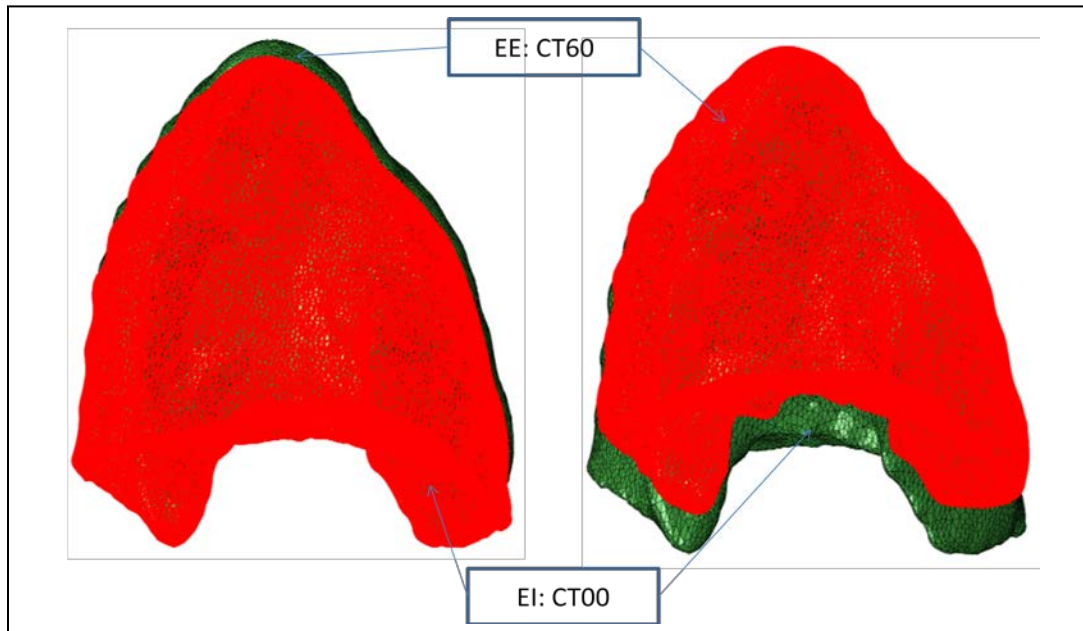


FIGURE III. 1: EE and EI states

This leads us to make an intermediate step in the process; we had not taken the beginning into account. We displace both geometries until both reach the same maximum height. This new modification was performed without problems using the calculation software used for image processing: MATLAB.

The later modification implies change in the problem approach that greatly simplifies the process: As a state of free breathing, the entire lung deformation occurs at the bottom. There is hardly any distortion at the top or side, as we discuss below. As a first approximation of our biomechanical model, we consider that what we had introduced at the beginning; fixing the root of the lung (see Figure II.1), is approximately equivalent to setting the same maximum height in both states.

Following the workflow in Figure I.1, after the allocation of EE and EI states, the application of loads and boundary conditions follows.

Boundary Conditions

The limiting geometry is supposed to be fixed at every moment. To make this possible, we apply no displacement neither rotation at all directions in all of its nodes.

Between the internal surface in the limiting geometry and the external surface in the internal volume, we define a frictionless contact condition which allows sliding between these surfaces due to the internal fluid in the pleural cavity.

To define this condition, the surfaces' normal faces are defined in accordance with the contact condition we are enforcing, as shown in figure III.2

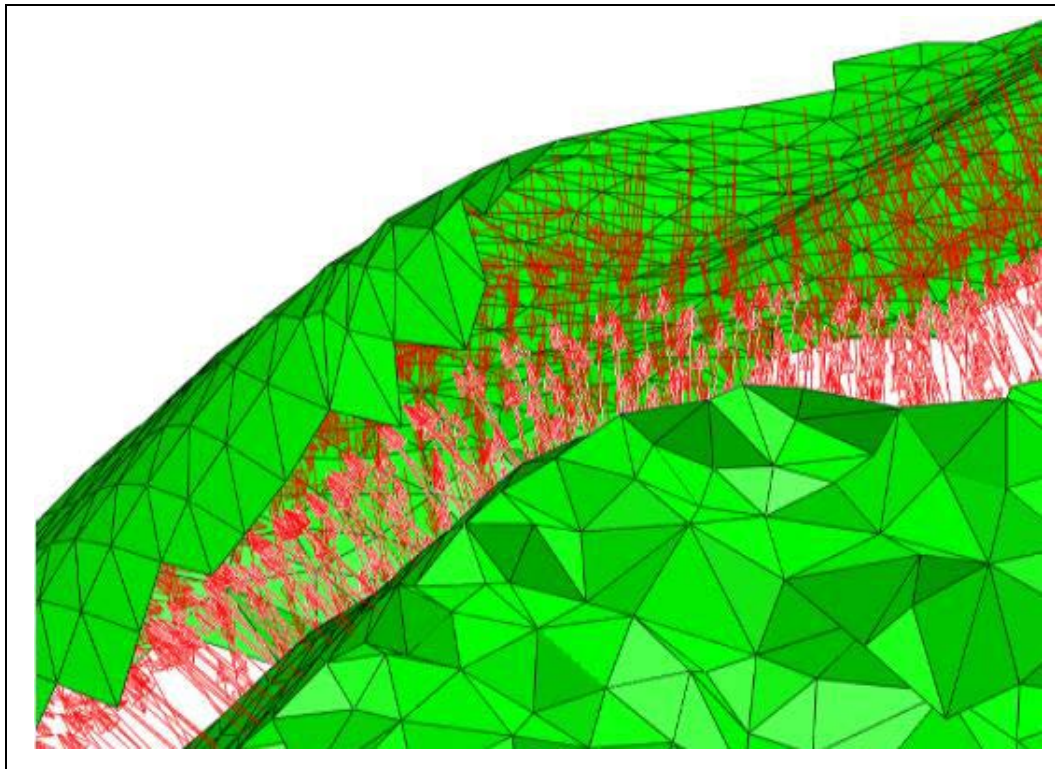


FIGURE III. 2: Normal vectors

Loads:

The loads applied in the geometry will be two negative pressures on the external surface of the volume that represents the EE estate.

- Pressure 1: value -0.016MPa , applied in the entire external surface of the EE state. This pressure correlates with pleural pressure as a force that acts on the lung surface.
- Pressure 2: value -0.012MPa . Is applied to the bottom surface, and represents the force generated on the lung when the diaphragm shrinks.

In figure III.3 we can see pressure 1 applied at all external surface in the lung in the left lateral. In the right lateral, the lung surface on which pressure 2 is applied is shown.

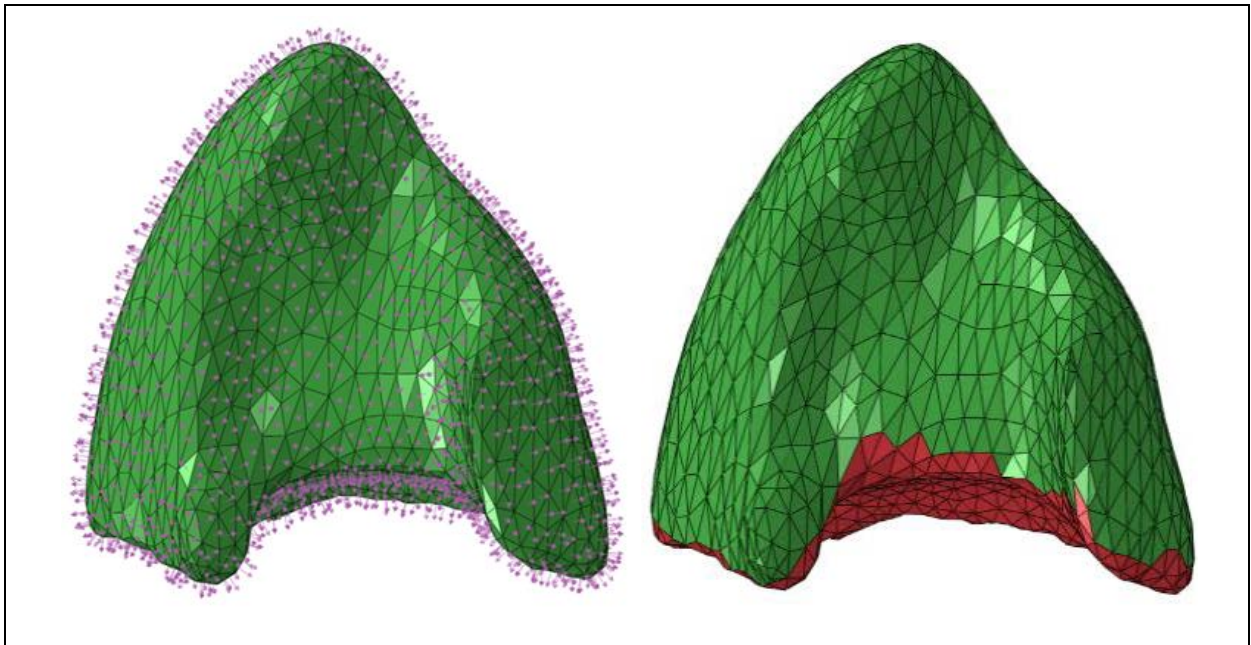


FIGURE III. 3: Pressure 1 and bottom surface.

Pressure 1 applied in the external surface of the lung in the right side, and in the left side bottom surface of the lung.

The simulation process consists of applying the pressures to the lung with the boundary conditions already imposed. As a result of pressures 1 and 2, the lung expands, reaching a geometry that represents the final state. Once both surfaces are in contact the inner surface slides on the external surface, the movements of which are completely restricted.

2. SIMULATION RESULTS

We use ABAQUS/CAE v6.10 programs for solving our numerical model. The simulation is carried out on a desktop computer and takes 14 minutes to complete.

Different output variables are obtained when the process ends. First is the displacement vector, \mathbf{u} , obtained directly from the discretized equations system seen in part II.2. Finite Elements.

Figure III.4 is a qualitative view of the displacement vector field obtained. The arrows are pointed at the final position of every node after the simulation process. The length of the arrows is proportional to the modulus of the displacement vectors.

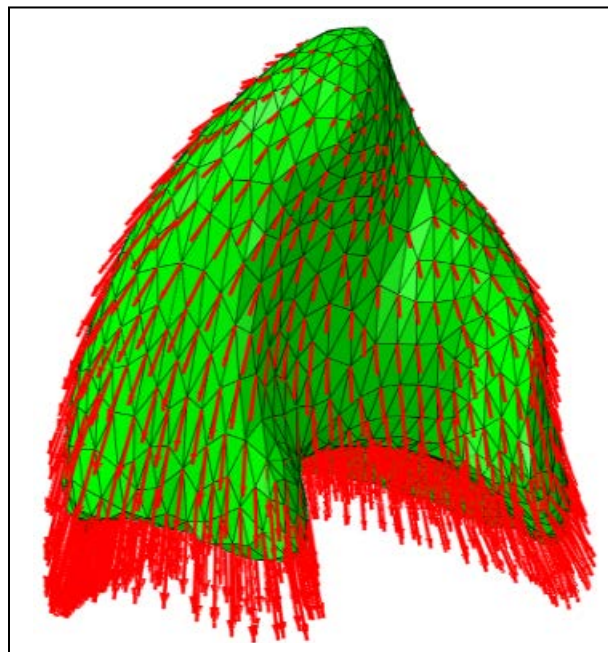


FIGURE III. 4: Displacement vectors

After looking at figure III.4, we can affirm that on the lung's top and lateral, no relevant displacements are obtained. Thus we can confirm our assumption that deformation primarily occurs in the bottom part of a lung during free breathing.

Both geometries are very close in the initial situation; the lung expansion is not allowed on the top due to the proximity of the limiting geometry. The displacement field is so small that is hard to appreciate.

The displacement vector modulus is useful to inform about the magnitude of the movements. In figure III.5 we can see a colorwash for \mathbf{u} .

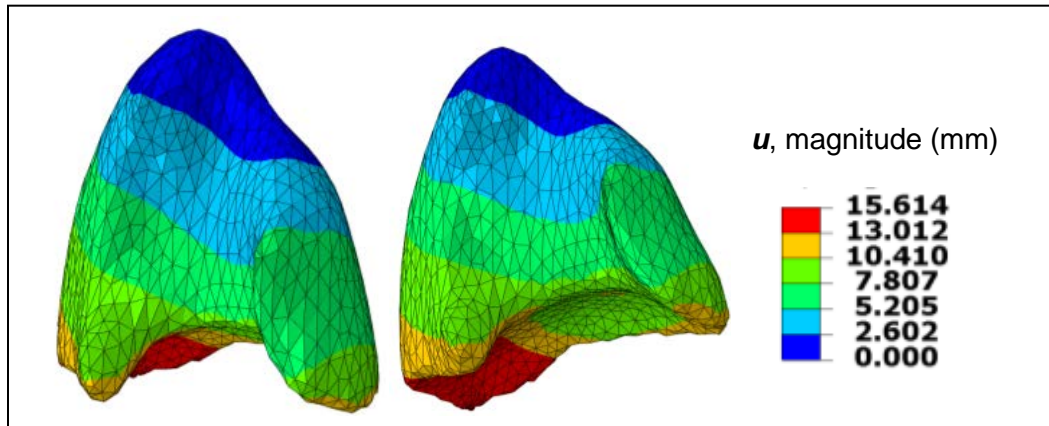


FIGURE III. 5: Displacement field magnitude

In figure III.5, we can see the modulus of the displacement field for the two different positions of the lung. Following the legend, points in dark blue areas have zero displacement or a displacement lower than 2.602mm. These are points on the top of the lung as we saw in figure III.4.

On the other hand, the maximum displacement is represented by the red color, which is found mainly on the bottom part of the lung. This is consistent with our prediction. The maximum displacement registered reaches 15.614mm. Despite of the high value reached, we do not know if the final positions of the nodes are in contact with the limiting geometry. In order to find this necessary information, we represent other output variable as a colorwash.

The new variable is known in the software as “**contact open**”, and gives an idea of the contact between two surfaces. If it is “open”, then there exists a gap or a very small separation. The opposite of having a contact open is penetration. Penetration occurs when both surfaces are inside each other. Penetration is represented as a negative contact open. Figure III.6 shows a colorwash of this variable.

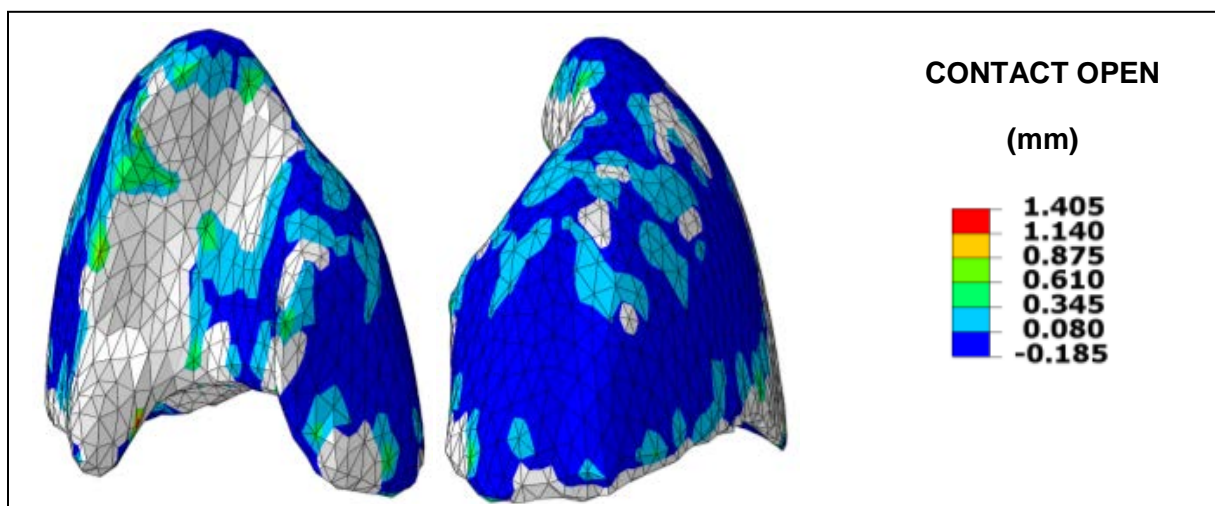


FIGURE III. 6: Contact open

In red we can see the maximum contact open detected at 1.405mm. If the distance between both surfaces is bigger than this value, the software will not detect the distance as a “contact”. The corresponding color for this situation is gray.

The result we have obtained for the variable open contact contains nodes that are not in contact with the limiting surface of the lung. This can be seen on the right side of the figure III.6, as the gray areas in the inner side of the organ.

Conversely, there are also many areas in dark blue, which indicate that the surfaces are in perfect contact (contact open = 0), or even a small penetration occurred between the surfaces. Although penetration is not desirable, it is not very alarming to due to its minimal intrusion (< 0.2mm).

Of more concern is the effect on the points for which the variable contact open is grayed. It is not possible to know if the distance between the two surfaces with respect to these points is significant or not. In other words, it is not possible to determine how far away the lung is from its final geometry. We can only ensure that the distance between the limiting geometry and the lung is greater than 1.405mm.

However, what if it is safe in view of the results is that it might be possible to modify the model to achieve a higher proportion in the final geometry.

PART IV: COMPARISON WITH OTHER TECHNIQUES

The displacements of the nodes of the mesh obtained with the finite elements software (ABAQUS/CAE) were exported to a computer analysis program (MATLAB).

This software will be used to interpolate the displacement field from the mesh level to the pixel level, thus obtaining an offset for each pixel that is within the geometrical lung. Once the displacement field is at the pixel level, the results are checked by comparison, in this case, with the deformable image registration method.

Before comparing the results from both techniques, the deformable image registration method must be explained as well as the similarities and differences with the FEM developed in this project.

1. DEFORMABLE REGISTRATION

Introduction:

Deformable Image Registration (DIR) is a specific type of geometrical transformation in medical image processing. By modifying the spatial relationships between voxels, an image can be shifted, rotated, stretched, shrunk, and manipulated to align similar scenes or objects.

To accomplish any of these, each voxel corresponding to an input spatial coordinate, (x, y, z) , must relocate to a voxel of an output spatial coordinate, (t, u, v) . The transform is a function that relates the spatial coordinates of these voxels,

$$(x, y, z) = T\{(t, u, v)\} \quad (\text{Eq.IV.1})$$

describing the differentiable gradient map that modifies their spatial relations in a manner that the user desires.

The main idea has been described in the above lines, but to understand the results and compare with the FEM is necessary to explain, at least briefly, the whole process.

Process:

Deformable image registration allows elastic geometrical transformations to be generated and applied between two images fast and accurately. These transformations can be used to simulate a wide variety of anatomical positions and structures correlating to the images from which they arose.

There are several DIR methods, all of them are very similar, but we will focus in **demons'** algorithm.

Demons' algorithm was first introduced by Thirion for DIR in (15). Its basis is a theoretical thermodynamic paradox in which a “demon”, or entity capable of distinguishing between two states, decides and allows two types of particles to pass between a semi permeable interface until the two types of particles are distributed evenly on each side of the interface. Basically all particles of the same type end up on one side of the semi permeable interface (15) (16). Its conjunction with medical imaging comes in an algorithm in which a “demon” distinguishes how a deformable model of voxels, a 3D moving image data set, deforms to a static model, or a 3D static image data set.

The gray level values (intensity) of each voxel correspond to the different densities of materials comprising the human anatomy. Iso-intensities represent the various tissues, organs and structures of patient's anatomy. A “demon” moves the deformable models voxels until their intensities accurately represent the static model voxels intensities.

In (15) and (16) the authors propose a mathematical algorithm to get the spatial displacement vectors based on the voxels intensity values.

In our application, the two images will represent the same observable patient features in 3D space (tissues, organs, bones) described at two independent time coordinates. In our case, the 3D data sets are two phases from the 4D CT described before. i.e. at the same initial and final states used in FEM. (EE and EI).

The image we wish to match to another will be defined as our moving or model image M, (EE state) while the image we are matching to will be defined as our static or scene image S (EI state).

We consider M (EE) to be a deformable 3D object whose voxels will relocate to the corresponding voxels of S (EI). The intensity values will remain constant as the M(P) voxel are either moved or drawn into the S(P) voxels position to match the deformable model contour since the density of tissues, organs and structures remains static.

Applying this to Thirion's original equation the displacement vectors can be described as

$$d\vec{r} = \frac{(I_m - I_s)\vec{\nabla}I_m}{(\vec{\nabla}I_m)^2 + (I_m - I_s)^2} \quad (\text{Eq.IV.2})$$

where I_m , I_s represent the CT intensities; $\vec{\nabla}I_s$ represent the gradient of the static image and $d\vec{r}$ represents the displacement vectors between the two images intensities.

After applying this procedure, displacement field is obtained. Deformable registration displacements are only localized where a gray level change takes place, in contrast with FEM, where the voxels' movement are due to external loads applying to the elastic model.

The DEMONS method is beyond the scope of this research project. In this document, it is only presented to get a second source of information of the displacement field, and as a way to verify and measure errors in the FEM results.

2. COMPARISON

Once DEMONS displacement field $U_{\text{DEMONS}} = U(X,Y,Z)$ and FEM displacement field $U_{\text{FEM}} = U(X,Y,Z)$ have been calculated, we proceed to the comparison of the results. Since the real displacement field is unknown and both methods are only an approximation of the organ's real movement, a single results comparison would be insufficient.

Following the evaluation of the modeling accuracy developed in the literature (2), (12), (11); a set of inner and outer lung **landmarks** or reference points were identified in the 4D CT image data by a medical physics expert.

The identified landmarks are located at easily recognized points within the lung geometry, for example prominent bifurcations of the bronchial tree. Eight landmarks were identified, and they are shown in the figure IV.1.

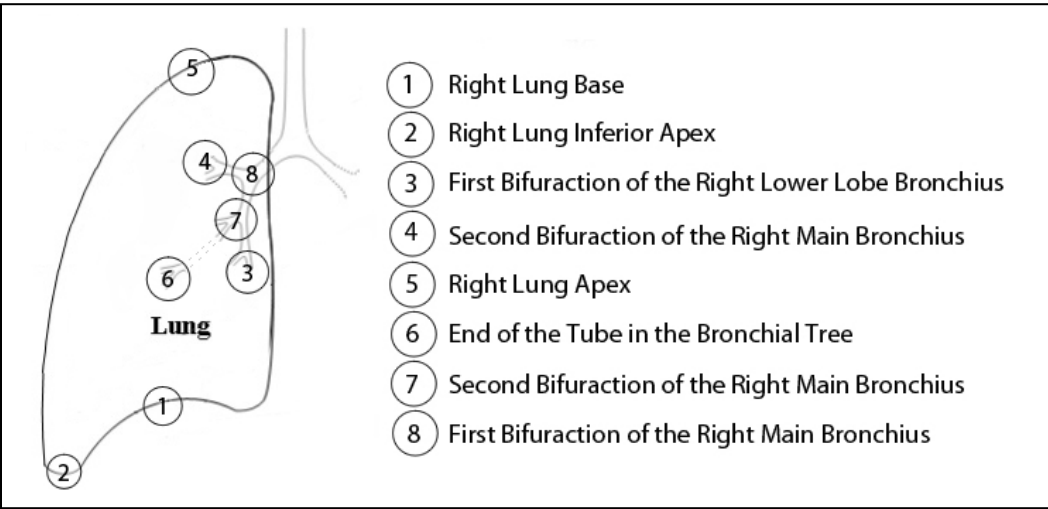


FIGURE IV. 1: Landmarks

Simplified2D sketch of the approximate position of every landmark.

The medical expert can localize the landmarks in both the EE and EI states. The differences of the coordinates at EE and EI positions from the 4D CT, give us the real displacement of these points. In the table IV.1 can be seen the values.

		x (pixel)	y (pixel)	z (pixel)	Δx (mm)	Δy (mm)	Δz (mm)	REAL u (mm)
Inmrk 1	ee	150	298	56				
	ei	150	298	61	0	0	12.5	12.5000
Inmrk 2	ee	119	256	57				
	ei	117	256	61	-1.9532	0	10	10.1890
Inmrk 3	ee	183	295	42				
	ei	184	295	45	0.9766	0	7.5	7.5633
Inmrk 4	ee	180	287	34				
	ei	178	284	37	-1.9532	-2.9298	7.5	8.2855
Inmrk 5	ee	174	256	10				
	ei	175	256	10	0.9766	0	0	0.9766
Inmrk 6	ee	174	235	47				
	ei	175	242	43	0.9766	6.8362	-10	12.1527
Inmrk 7	ee	186	312	49				
	ei	186	304	52	0	-7.8128	7.5	10.8300
Inmrk 8	ee	186	247	34				
	ei	184	249	37	-1.9532	1.9532	7.5	7.9925

TABLE IV. 1: Landmarks positions at EE and EI and displacement vectors

To perform the pixel/length calibration, pixel size and the slice thickness, (aka the voxel size), has been taken into account.
That is (0.9766 x 0.9766 x 2.5 mm3)

Based on the landmarks' locations at EE, we predicted the landmarks' position at EI by adding the corresponding displacement vectors given by the computed displacement field, \mathbf{u} , in both methods: DEMONS and FEM. These displacement vectors are shown in mm table IV.2.

To compare the results, we use 8 landmarks of which are known:

- The displacements in the 4D CT. This is what we call real displacement.
- The displacements in the finite element model. (FEM).
- The displacements given by deformable registration algorithm. (Demons)

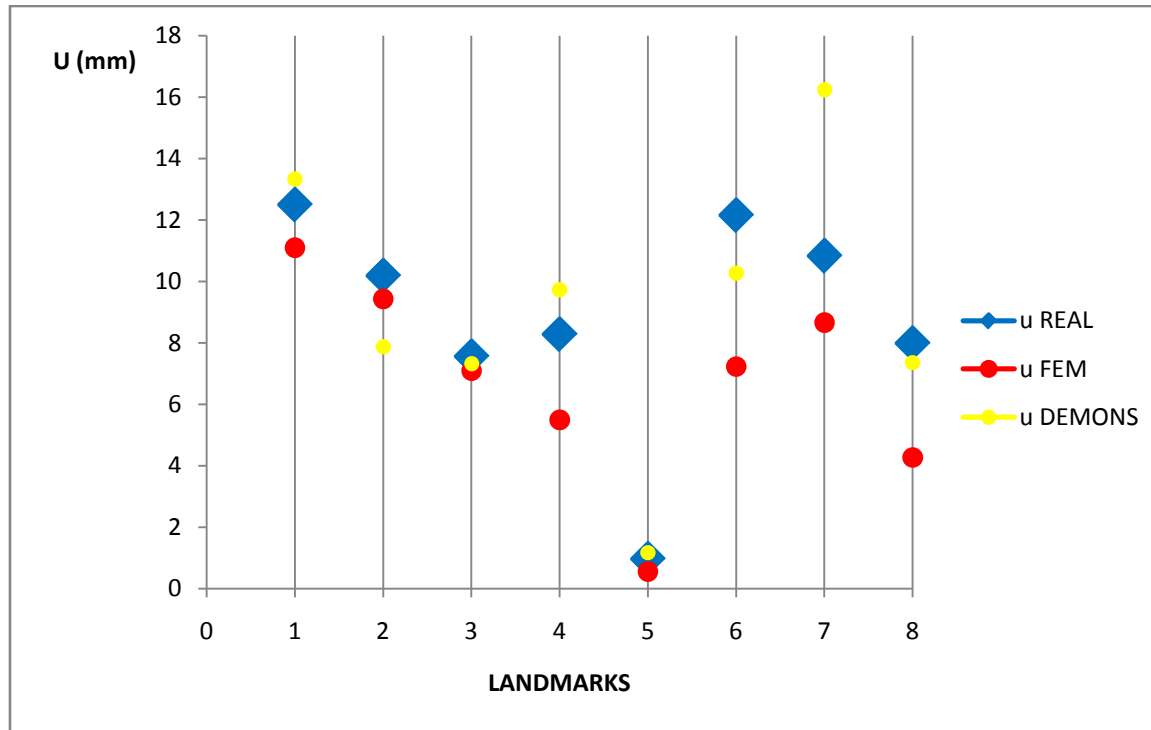
To have a quantitative measurement of the accuracy of both models, the differences between the displacements of all landmarks in each model and the real displacements are calculated.

Table IV.2 shows the displacement magnitudes for all landmarks identified in the 4D CT. The three first columns are the REAL, FEM and DEMONS displacements respectively in mm. The two next columns contain the errors in mm between the corresponding method and the real displacement, calculated as: $\text{error}(\text{mm}) = U_{\text{METHOD}} - U_{\text{REAL}}$.

	REAL u (mm)	FEM u (mm)	DEMONS u (mm)	error FEM (mm)	error DEMONS (mm)
Inmrk 1	12.5000	11.1006	13.3319	-1.3994	0.8319
Inmrk 2	10.1890	9.4347	7.8709	-0.7543	-2.3180
Inmrk 3	7.5633	7.0960	7.3237	-0.4673	-0.2396
Inmrk 4	8.2855	5.4991	9.7237	-2.7864	1.4383
Inmrk 5	0.9766	0.5614	1.1825	-0.4152	0.2059
Inmrk 6	12.1527	7.2326	10.2677	-4.9201	-1.8849
Inmrk 7	10.8300	8.6642	16.2312	-2.1658	5.4011
Inmrk 8	7.9925	4.2716	7.3674	-3.7209	-0.6251

TABLE IV. 2: Comparison of the displacements

Data in table format is not easily comparable. In order to analyze the results in a visual manner, we show them in graph IV.1.



GRAPH IV. 1: Landmarks displacements comparison

The graph depicts the landmarks' movements for each of the different methods. In blue and with a larger marker, the real displacements are represented. We chose a higher marker to differentiate the real displacement from the rest. The red and yellow markers represent landmarks' movements obtained through FEM and DEMONS methods respectively.

From these results, we see that for landmarks 1, 2, 3 and 5, the displacements obtained by FEM are very close to the actual displacement obtained through 4D CT. Errors obtained in absolute value are 1.3994mm, 0.7543mm, 0.4152mm, 0.4673mm respectively.

In contrast, for landmarks 4, 6, 7 and 8, errors in the displacements obtained using FEM are 2.7864mm, 4.9201mm, 2.1658mm, and 3.7209mm in absolute value, respectively. These last four landmarks also show a common feature: they are all landmarks located inside the lung.

With the DEMONS method something similar happens. The errors are higher in the internal landmarks, reaching an error of 5.4011mm in landmark number 7, located on the second main bifurcation of the bronchial tree. This result is to be expected for a method based on the image gray level, since, as seen in the figures II.2 and II.3, the lung is filled with air, thus the image we see is completely black in the inside.

However, as announced in the beginning, this method is beyond the scope of this project and we will not discuss the results any further.

Returning to the results obtained by FEM, the landmarks located at the surface of the lung tend to have smaller errors relative to the real model. This confirms a previous hypothesis brought in light of the simulation results: the lung reaches its limiting geometry in most of the surface points.

Regarding the inner points, we can justify the lack of precision of the model due to the assumption of homogeneous properties of the lung.

Another possible source of error could be due to the reliability of the displacements that we considered real. These observations come from images that already have errors (e.g. image artifacts). Additionally, points are manually selected by a human observer who leaves room for error.

As a final note, it is important understand that all displacements obtained by FEM have negative error. (All are below the blue marker on the chart IV.1), the displacement is always less than real. This may be because the mechanical properties assigned in the lung are too rigid and do not allow the movement to reach its set value. Another possible cause could be the choice of the negative pressure applied in the surface; by applying more pressure; the solid could deform more.

Both ideas will be taken into account in the following suggestions for improvements to our model.

PART V: CONCLUSIONS AND FUTURE WORKS

At this point we discuss the most relevant aspects of a biomechanical model of the lung: its utilities and applications as well as the framework in radiotherapy in which it proves most useful.

1. SIGNIFICANCE AND INNOVATION OF A BIOMECHANICAL MODEL OF THE LUNGS

The first innovation was introduced at the beginning of this paper: It develops a framework for dosage calculation in variable and mobile anatomy. Currently, all dosage calculations models are based on static images of the lung and thorax. Consequently, the actual dose delivered to the tumor during the treatment is not exactly known.

With our research, we are one step forward to creating real time, computed anatomy, constituting a key step in Adaptive Radiation Therapy (ART) and allowing for treatment corrections when there is a discrepancy between delivered and planned dosage amounts.

Knowing the exact amount of radiation is a very important goal, but it also solves one of the biggest problems in radiotherapy of mobile tumors: the lack of accurate knowledge of tumor

position during treatment. The knowledge of tumor position is an essential requisite for providing radiation therapy. Although many motion management techniques have been developed, they are not accurate under irregular breathing conditions because the models assume regular breathing patterns. Since biomechanical properties do not change under different breathing conditions, the proposed model should accurately give the position of the tumor for any breathing pattern.

The biomechanical model of the lung represents a solution for motion management in radiation therapy, which may significantly reduce normal tissue toxicity due to overdose and/or improve tumor control. Breathing motion is one of the contributing factors in dose escalation in radiation therapy of tumors of the thorax and abdomen, specifically in the lung tumor. Because the tumor position changes, larger margins are added to the treatment volume in order to cover the tumor at all times. This leads to larger doses to a healthy lung along with the associated toxicity. With the biomechanical model proposed, it is possible to locate the position of the tumor accurately, allowing a more precise treatment to be delivered.

A biomechanical model of the lung incorporates tumor deformation and organ motion. Most of the work in respiratory motion models falls in the category of a single point motion calculation. While it is essential to study the motion of a single point of interest, we should aim to find the motion of the entire lung, which might be important in some cases. Tumor deformation, long neglected until now, will be captured in the proposed model.

Finally we should not discount the possibility of extending the model. Using the biomechanical model of the lungs as a paradigm, it should be easy to extend our model system to other organs like the diaphragm, breast, abdomen, etc. Developing a finite element model of the thoracic region, utilizes a technique that can be used for other medical applications. The modeling of biomechanical tissue properties has gained considerable interest in a range of clinical and research applications. FE models can be used to model the relationship between different tissue types by applying displacements or forces. This can help to predict mechanical or physical deformations during surgical procedures and derive and quantify tissue properties from observed deformations.

2. HOW TO IMPROVE THE MODEL

Throughout the project we have discussed possible sources of error in the results. At this point we will discuss all of them.

First, a possible improvement would be a using a smaller mesh. By refining the mesh, we would get more detail in the geometry of the 3D volume, which would help us find a more precise location of the interior points of the lung, landmarks and tumors.

Another possible improvement to our model would be a change in the fundamental assumptions we have used to model the tissue. We assumed lung tissue is a homogeneous medium. In reality, the lung contains different structures such as the bronchis, brochiolis and so forth. In more in-depth research we will drop the simplified assumption of a homogeneous medium and take into account heterogeneity of the lung medium. For example, the model could include the bronchial tree, despite the fact demonstrated in (2) that its inclusion has little significance, including the bronchial tree could improve the result. As seen in the previous part, the landmarks with larger errors are found inside the solid, which indicates that the interior does not quite imitate the actual behavior of the lung interior.

Additionally, we assume the lung to be isotropic linear elastic. This requires a dimensioning of the elastic constants: Elastic modulus, and Poisson's ratio, ν . In previous literature, several values of E and ν are listed (see table II.7).

Young's modulus and Poisson's ratio open a wide field for research. Measuring E and ν in living tissues is a difficult task. Finding appropriate values, which correspond to real constants, requires the development of techniques for measuring these parameters. Zhang T. et al. in (9) for this purpose are based on the compliance (C), which represents the ratio of air volume variation to the related air pressure variation. This is obtained from the experiments in the respiratory physiology analysis performed in a hospital by a medical expert. From the bulk modulus (K) definition, they associate the Young's modulus and the Poisson's ratio with the initial volume (V_i) according to the equation (Eq.V.1).

$$K = \frac{E}{3(1 - 2\nu)} = \frac{V_i}{C} \quad (\text{Eq.V.1})$$

Poisson's ratio is assumed to not affect the results significantly, thus it is fixed at 0.33. C is obtained from the experiments and V_i is a well known value.

Although the accuracy of this method is not assured, further research could be the basis for a possible case study.

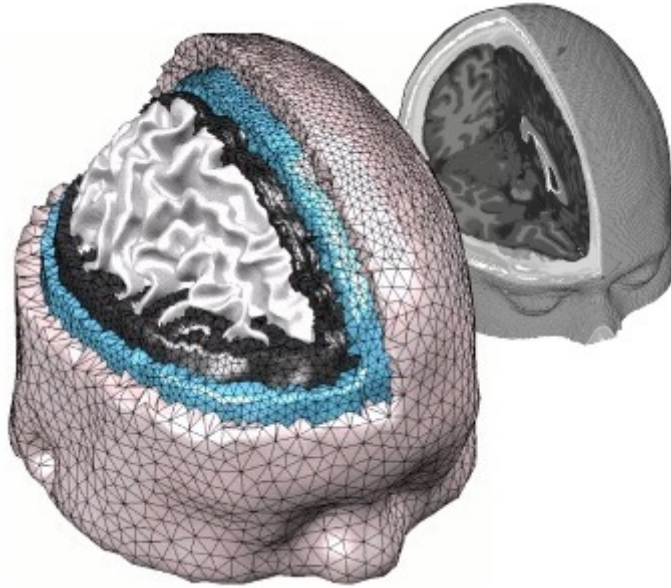
During the project we have justified why we do not want the "real" value of the elastic properties. The use of an unreal value is feasible in the first, primitive model, but future

enhancements of the model will include more organs inside the chest cavity, and elastic mechanical properties between different organs gain importance.

As already stated, this is an initial model; there are still improvements to be made for the model to realize its proper application of treating patients. Enhancements must be made before it is put in use. For example, the outer surface of the patient could be modeled so that the movement of the chest of a breathing patient can be modeled. The movement of the lungs could be obtained and with them, the displacement field inside the organ. This will avoid all problems involving the application of a pressure unknown in advance and lead to more accurate results. Additionally, the technique could incorporate the use of non-invasive imaging. By using surface imaging and a biomechanical model to derive tumor position from the surface image, the patient can avoid any kind of invasive procedure.

APENDIX A:

iso2mesh – a free 3D surface and volumetric mesh generator



`iso2mesh` is an open-source software for Matlab/Octave developed by Qianqian Fang at the Optics Division, Martinos Center for Biomedical Imaging, Massachusetts General Hospital/Harvard Medical School.

`iso2mesh` is a free 3D mesh generation toolbox. It incorporates a number of free mesh processing utilities, and It capable of producing quality 3D tetrahedral mesh or triangular surface directly from binary, segmented or gray-scale medical images. The structure of the software is highly modularized, optimized for processing efficiency.

All codes in `Iso2mesh`, are based on CGAL algorithms. CGAL means Computational Geometry Algorithms Library and is an open Source Project to provide easy access to efficient and reliable geometric algorithms in the form of a C++ library. It offers data structures and algorithms like triangulations, Voronoi diagrams, Boolean operations on polygons and on polyhedra, arrangements of curves, mesh generation, geometry processing...

`Is2mesh`, as we make used of it, is a particularization to MATLAB/OCTAVE of CGAL libraries.

APENDIX B:

Planning and Budget

In this part we explain the steps carried out during this project developing, as well as a budget with all costs necessities in the procedure.

This project started on 9th of April 2011, and finished 31st of August 2011. The total duration was 139days. Work is divided in several stages, and has been done by a senior engineer and the supervision of a senior engineer. It must be borne in mind that both are working in a multidisciplinary team, with experts in medicine and engineer fields.

Following, the main stages are summarized with the duration in parenthesis.

1. **Documentation and data and supplies acquisition. (30 days).** During this time, the senior engineer was reading documentation about the project; meanwhile, the 4D CT images are being taken by an expert and the equipment are being acquired. (Computer and software required)
2. **Extract images and mesh the geometry (7 days).** Create the lung meshed.
3. **Smoothing the mesh (20 days).** All smoothing processes were tried with different weighting factors.
4. **Images processing (15 days).** Joining both geometries and converting in to a input file for Abaqus.
5. **Abaqus documentation. (20 days).** Reading abaqus/cae manual as well as carrying out some didactics examples to understand the software.
6. **Numerical model. (7 days).** Assigning properties, loads and boundary conditions to the geometry.
7. **Simulations. (10 days).** Running simulations which solve the problem.
8. **Obtaining results. (20 days).** Importing the results to Matlab and obtaining the displacement field.
9. **Comparison results with other techniques. (10 days).** Comparing with demons method.

The next figure shows all this processes represented in a Gantt Diagram. In it we can see all succession of tasks, and the date they were carried out. It is important to mention the labor of the arrows: they indicate whether a task can start when the predecessor tasks start or finish.

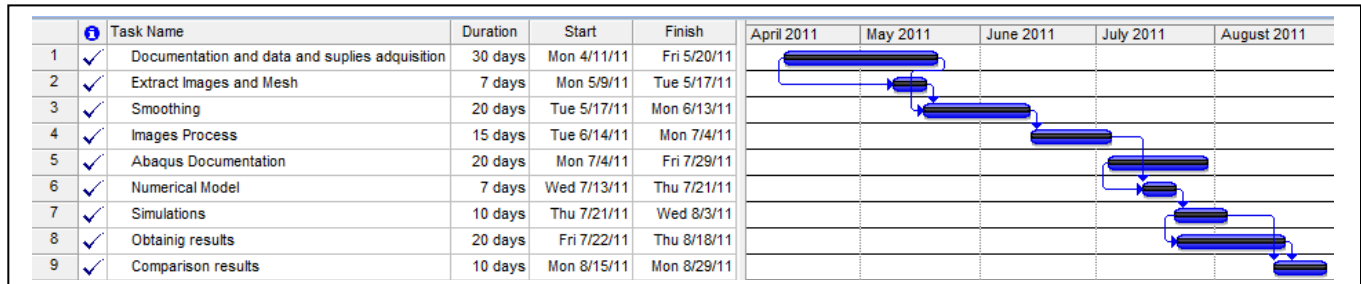


FIGURE A.B. 1: Gantt Diagram of the process

In the next chart, the budget for the project is presented. Several assumptions are taken before elaborating the total costs. Below these conditions are presented, in order to explain the hypothesis made for the budget.

- All cost are calculated in US dollars
- Workday is 8 hours
- One month is 20 workdays
- Engineer dedication is computed as men per hour. Where 1 man per hour is 131.25 hours of work.
- Equipments amortization is consider as the next equation indicates:

$$\frac{A}{B} \cdot C \cdot D \quad (\text{Eq.A.B.1})$$

Where

- A Number of months using the equipment
- B Depreciation period
- C Equipment Cost
- D Percentage of use dedicated to project

- 5 years are taken as a depreciation period in hardware
- 12 months are taken as a depreciation period for software licenses
- Any other equipment used in the project which doesn't appear in the budget is assumed to be already amortized, as well as software licenses.
- No task is outsourcing.



UNIVERSITY CARLOS III OF MADRID

Higher Polytechnic School

PROJECT BUDGET

1.- Author:

Gloria Núñez Márquez

2.- Departament:

Thermal and fluids engineering

3.-Project description

- Title	Towards a biomechanical model of the human lung
- Duration (months)	5
- Indirect cost rate	20%

4.- Overall budget of the project:

47,073 US Dollars

5.-Budget break down (Direct Costs):

PERSONNEL

Last name, First name.	ID number	Category	Dedication (men per months)	MpM cost	Cost (Dollar)
Last name, first name	xxxxxxx-X	Senior Engineer	1.22	5,895.54	7,192.56
Last name, first name	xxxxxxx-X	Engineer	6.1	3,703.17	22,589.34
Last name, first name	xxxxxxx-X	Medical Physics	0.61	3,703.17	2,258.93
					32,040.83

Total

EQUIPAMENTS

Description	Cost (Dollar)	% of total use for this project	Dedication (months)	Deprec. Time	Cost
Desktop computer	3,000.00	100	5	60	250.00
Matlab license	1,300.00	52	3	12	146.47
Abaqus license	2,000.00	41	2	12	140.08
Total					536.55

TASKS OUTSOURCING

Description	Company	Cost
	Total	0.00

OTHER DIRECT COSTS

Description	Units	Cost
Plane ticket	1	1,100.00
Host	5	3,350.00
Diets	100	2,000.00
Visa	1	200.00
	Total	6,650.00

6.- Costs Summary

Total Costs budget	Total cost budget
Personnel	32,041
Amortization of equipments	537
Tasks outsourcing	0
Other Direct Costs	6,650
Indirect costs	7,845
Total	47,073

TABLE A.B. 1: Budget

The final budget for this project rises to FOURTY SEVEN AND SEVENTY THREE DOLLARS.

Leganés, X of October 2011

The project engineer

Sign. Gloria Núñez Márquez

REFERENCES

1. **Gray, Henry.** *Anatomy of the human body.* 1918.
2. *Deformable image registration of heterogeneous human lung incorporating the bronchial tree.* **Al-Mayah, Adil, Moseley, Joanne y Velec, Mike.** [ed.] 4571. 2010, Medical Physics, Vol. 37, pág. 4560.
3. *Conforming Delaunay triangulations in 3D.* **Cohen-Steiner, D., Colin de Verdière, E. y Yvinec, M.** 2004, Computational Geometry, Vol. 28, págs. 217-233.
4. *Delaunay refinement algorithm for triangular mesh generation.* **Shewchuk, J. R.** 2002, Computational Geometry, Vol. 22, págs. 21-74.
5. *A generic software design for Delaunay refinement.* **Rineau, L. y Yvinec, M.** 2007, Computational Geometry, Vol. 38, págs. 100-110.
6. **SIMULIA.** ABAQUS/CAE user's manual. *Abaqus 6.10 documentation.* [Online] <http://abaqusdoc.ugalaxy.ca/v6.9/books/usi/default.htm>.
7. *Comparison of fundamental mesh smoothing algorithm for medical surface models.* **Bade, Ragnar, Haase, Jens y Preim, Bernhard.** 2006, Simulation and visualization, págs. 289-304.
8. *Improved laplacian smoothing of noisy surface meshes.* **Vollmer, J., Mencil, R. y Muller, H.** 1999, Eurographics, págs. 131-138.
9. *Technical Note: A novel boundary condition using contact elements for finite element based deformable image registration.* **Zhang, T., Orton, N. P. y Mackie, T. R.** 2004, Medical Physics, Vol. 31, págs. 2412-2415.
10. *Analysis of deformable image registration accuracy using computational modeling.* **Zhong, H., Kim, J. y Chetty, I. J.** 2010, Medical Physics, Vol. 37.
11. *Accuracy of finite element model-based multi-organ deformable image registration.* **Brock, K. K., y otros.** 2005, Medical Physics, Vol. 32, págs. 1647-1659.
12. *Modeling respiratory lung motion - a biophysical approach using finite element methods.* **Werner, Rene, y otros.** 2008, Medical Imaging, Vol. 6916.

13. *Towards a model of lung biomechanics: pulmonary kinematics via registration of serial lung images.* **Sundaram, T. A. y James, C.** 2005, Medical Image Analysis, Vol. 9, págs. 524-537.
14. *Modeling respiratory motion for cancer radiation therapy based on patient specific 4D Ct data.* **Eom, J., Shi, C. y George, X.** 2009, Lecture Notes in Computer Science, Vol. 5762, págs. 348-355.
15. **Thirion, J. P.** *Fast non-rigid matching of 3D medical images.* Antibes, France : Institut National de Recherche en Informatique et en Automatique, 1995.
16. *Image matching as a diffusion process: An analogy with Maxwell's demons.* **Thirion, J. P.** 1998, Medical Image Analysis, Vol. 2, págs. 243-260.
17. **Chiras, Daniel D.** *Human Doby Systems: Structure, function and enviroment.* Sudbury, MA : Jones and Bratlett, 2003.
18. **Fung, Yuan Cheng.** *Biomechanics: Mechanical properties of living tissues.* New York : Springer-Verlag, 1993.
19. **Timoshenko, Stephen.** *Theory of elasticity.* New York - Toronto - London : MacGraw-Hill, 1951.
20. *Feasibility of deformation independent tumor tracking radiotherapy during respiration.* **Kim, S. y Yoon, M.** 2011, Medical Physics, Vol. 36, págs. 78-84.
21. *Elasticidad y Ressitencia de materiales.* **Astriz Suárez, M. A.** s.l. : Publicaciones de la Escuela Técnica Superior de Ingenieros Aeronáuticos, 1991.
22. **ACR-American College of Radiology and RSNA-Radiological Society of North America.** RadiologyInfo - The radiology information resource for patients. "*Computed Thomograpy*". [Online] <http://www.radiologyinfo.org/sp/>.
23. **Fang, Qianqian.** Iso2mesh: a free 3D surface and volumetric mesh generator for Matlab/Octave. [Online] 2009. <http://iso2mesh.sourceforge.net/cgi-bin/index.cgi>.
24. **Scribd.** Human respiratory system. [Online] <http://scribd.com>.
25. **Company, General Elentric.** GE Healthcare. [Online] <http://www.gehealthcare.com>.
26. **General Electric Company.** GE Healthcare. [Online] <http://www.gehealthcare.com>.